

# **Characterization of Self-Magnetic Pinch (SMP) radiographic diode performance on RITS-6 at Sandia National Laboratories: 2) Coupling between the Inductive Voltage Adder (IVA) and the SMP load.**

T. J. Renk, B. V. Oliver, M. L. Kiefer, T. J. Webb, J. J. Leckbee, M. D. Johnston, S. Simpson, and M. G. Mazarakis

Sandia National Laboratories, Albuquerque, NM 87185, USA

Corresponding Author: T. J. Renk, email: [tjrenk@sandia.gov](mailto:tjrenk@sandia.gov)

## **ABSTRACT**

The self-magnetic pinch (SMP) diode is a type of radiographic diode used to generate an intense electron beam for radiographic applications. At Sandia National Laboratories, SMP was the diode load for the RITS-6 Inductive Voltage Adder (IVA) driver operated into a magnetically insulated transmission line (MITL). The MITL contributes a flow current in addition to the current generated within the diode itself. Extensive experiments with a MITL of 40 ohm load impedance (T. J Renk *et al*, Phys. Plasmas xx xxx) indicate that the additional flow current leads to results similar to what might be expected from a conventional high-voltage interface driver, where flow current is not present. However, when the MITL flow impedance was increased to 80 ohms, qualitatively different diode behavior was observed. This includes large retrapping waves suggestive of an initial coupling to low impedance, as well as diode current decreasing with time even as the total current does not. A key observation is that the driver generates total current (flow + diode) consistent with the flow impedance of the MITL used. The case is made in this paper that the 80 ohm MITL experiments detailed here can only be understood when the IVA-MITL-SMP diode is considered as a total system. The constraint of fixed total current plus the relatively high flow impedance limits the ability of the diode (whether SMP or other type) to act as an independent load.

Key words: inductive voltage adder (IVA) accelerators, electron beam focusing, high-voltage techniques, magnetic insulation, impedance behavior in high-power anode-cathode (A-K) gaps, dose-rate diagnostics

## I. INTRODUCTION

The Self-Magnetically Pinched (SMP) diode is a form of intense relativistic electron beam diode that was developed specifically as a potential x-ray source for short-pulse flash X-ray radiographic interrogation of dynamic experiments [1,2]. An electron beam is focused to as small a point as possible, in order to function as a point-source for x-ray interrogation of an object. The target consists of high-atomic-number material (e.g. tantalum), which the electron beam impinges upon to produce an intense pulse of bremsstrahlung X-rays. The radiographic resolution is determined by the spot size of the x-ray source.

The SMP diode was operated as a diode load in negative polarity for the six-cavity Radiographic Integrated Test Stand (RITS-6) pulsed-power accelerator at Sandia National Laboratories. The RITS-6 architecture is that of an Inductive Voltage Adder (IVA) feeding a magnetically insulated transmission line (MITL) [3]. In a MITL, the electron field at the negative (center) electrode exceeds the threshold for electron emission, and the resultant self-insulated flow (behind an initial loss-front) represents current approaching the diode load over and above the current that is generated at the diode itself. The existence of MITL flow in an IVA leads to fundamentally different physics from that present in a vacuum line and high-voltage interface. In the latter, flow is not present. These flow electrons represent a complicating factor in characterizing the physics of the high-power diode fed by the IVA. The flow electrons occur separate from and in addition to currents flowing in the electrodes.

For a given energy delivered to the IVA, the output current and voltage in the MITL can be adjusted by varying the distance between the inner and outer conductors of the MITL. In practice, the outer conductor dimension is fixed, and the inner conductor radius is adjusted. From the ratio of the outer-to-inner diameter of the two conductors, the *vacuum impedance* of the MITL is determined and may be calculated [4]. The smaller the inner conductor dimension, the higher the vacuum impedance. Once the power pulse begins and MITL current flows, the effective impedance of the MITL is decreased by the added presence of the flow electrons. The resulting impedance is termed the *flow impedance*. The flow impedance of a MITL can be calculated by calculating the forward-going voltage, then dividing by the total current, which is linked to the voltage. The voltage can be calculated using the theory of Miller and Mendel [5], as modified more recently [6,7]. As the vacuum and flow impedance are raised (by shrinking the inner conductor dimension), the output voltage rises and the flow current decreases [8].

SMP experiments on RITS-6 have been performed at an output voltage from 3.5 to over 11 MV. To span this range, two different inner MITL conductors were used. The larger-diameter MITL is termed the “Lo-

Z MITL”, with vacuum and flow impedance values of 51.3 and 40 ohms, respectively. SMP shots were taken with output voltages from 3.5 to  $\sim 8.5$  MV with this MITL. The smaller-diameter MITL is referred to as the “Hi-Z MITL”, with respective vacuum and flow impedances of 102.8 and 80 ohms. Note that a) the flow impedance of the Hi-Z MITL is twice that of the Lo-Z MITL, and b) the ratio of flow to vacuum impedance is approximately 0.78 in both cases. Output voltages of up to an estimated 12 MV were generated on RITS-6 using the Hi-Z MITL. A schematic drawing comparing the two inner MITL dimensions is presented in Section II.

Characterization of SMP diode performance in RITS-6 experiments using the Lo-Z MITL is extensively discussed in a previous paper [9], with additional information available [10,11]. The geometry of the SMP diode will be schematically illustrated and diode dynamics discussed in Section II. Briefly, an intense electron beam is emitted from a small-diameter cathode and impinges on an anode in a non-pinching manner. The anode consists in part of high-Z material (tantalum), from which energetic photons are emitted through the bremsstrahlung process. The electron impingement causes a counter-streaming ion beam to form, which neutralizes the electron space charge, leading to a pinch formed on the anode which is the source of the small photon source spot size, the goal of a radiographic source. Optimum SMP performance is shown to occur with cathode diameter and diode anode-cathode (A-K) gap equal to each other (1:1 aspect ratio). For a given SMP voltage output, use of a smaller-diameter cathode can lead to reduced spot size, but can also result in a truncated radiation pulsewidth and dose (declines of up to 50%). The cause of this reduction can be ascribed either to A-K gap closure due to converging electrode plasmas [12], or [9,13] to inferred oscillations in angle of the electron impingement on the anode that are suggestive of some kind of beam instability that terminates the power pulse prematurely. The addition of DC heating and RF discharge cleaning of the diode region (not used in the experiments discussed in this paper) appears to result in stabilization of such beam oscillations, although this conclusion is tentative, due to the relatively few experiments having been performed.

The original SMP diode experiments were carried out in facilities at lower voltage, where the power flow was carried forward through a high-voltage interface instead of an IVA-MITL design. In a high-voltage interface, there is no electron flow coming forward. The discussion here of the SMP diode as a load for an IVA-MITL can be generalized to any kind of diode (bremsstrahlung, ion diode, for example). When the power pulse arrives at the diode load, the diode evolves in operation according to the physics specific to that diode. When an IVA-MITL is used instead of a high-voltage interface, the additional MITL flow current arriving at the diode constitutes a second system current in addition to the diode current.

The total current flow can be illustrated in Figs. 1a-c. The three schematic drawings there give a picture of the evolution of the MITL flow during the SMP power pulse. The hardware shown is a simplification of the SMP hardware to be further discussed in Section II. In Fig. 1a (Stage 1), the electron flow is initially diverted towards the outer MITL wall by the circular field shaper. During this time, current begins to flow through the SMP diode load (Fig. 1b, Stage 2). The resultant magnetic field from the rising diode current attracts the diverted flow towards the radiation axis, where it appears in the vicinity of the diode current (Fig. 1b, Stage 3). This picture of system current flow in Figs. 1 will be reinforced in the data discussions that follow in this paper. Well upstream of the hardware depicted in Figs. 1, the total (outer MITL) current is measured. This current includes both the inner electrode current and the electron flow (also called “sheath” current). As will be discussed in more detail in Section II, at Stage 3 in the power flow (Fig. 1c), the sheath flow approaches the anode side at a point close to (but not joining) the diode current. Current monitors placed in proximity to the anode are observed to measure almost the same current level as that measured upstream.

We will present an estimation process for the diode voltage (as opposed to the MITL voltage mentioned above) in Section III. Once the diode voltage can be estimated, a “total” system impedance  $Z_{\text{TOTAL}}$  is derived by dividing the diode voltage by the total current, measured either upstream, or (after Stage 3 occurs) at the anode wall near the diode. The diode impedance  $Z_{\text{DIODE}}$  is derived by dividing the diode voltage by the diode current (see Section II). Finally, the sheath current represents a “parallel” load current whose magnitude can be derived by the formula for two resistances in parallel:

$$1) \quad 1/Z_{\text{PARALLEL}} = 1/Z_{\text{TOTAL}} - 1/Z_{\text{DIODE}}$$

The importance of these derivations can be illustrated in Fig. 2, which plots  $Z_{\text{TOTAL}}$  for a collection of SMP shots taken with various diode configurations and with the Lo-Z MITL in place. The early part of the waveforms (before  $\sim 2.3 \mu\text{s}$ ) takes place in Stage 2 (Fig. 1b), before the sheath current approaches close to the anode axis (Stage3), and can be ignored. After this time, all the waveforms converge at approximately 40 ohms, before they slowly decrease due to a reduction in the effective A-K gap caused by converging electrode plasmas. A plot of various SMP shots taken with the Hi-Z MITL in place would show similar behavior centered around  $Z = 80$  ohms (see Sections VI and VII). Both 40 and 80 ohms are the flow impedances of the Lo-Z and Hi-Z MITLs, respectively.

This plot points to a fundamental aspect of current behavior in the coupled IVA-MITL-SMP diode system: the total current coming forward is consistent with the flow impedance of the MITL in place.

Thus, the total current available can be considered fixed. But the diode current evolves (Stage 2) independent of the additional sheath current. If then the diode current is set by the local diode physics, and the total current is fixed, then the system current required may be over-specified, leading to possible deviations in the diode current from what can be expected. In other words, the diode impedance may not be independently determined, but must be considered as part of a “system solution”. This will be illustrated in the data analysis in Sections VI and VII.

This paper addresses in detail the coupling between the IVA-MITL and a diode load, with the SMP diode used as a test-bed for a typical diode load. Some discussion will be given to the behavior of an ion diode load [14,15] in Section III, in which similar behavior to that seen with the SMP diode will be noted. It must be pointed out here that while simulations of SMP dynamics are not the primary focus of the present paper, extensive simulations of the SMP with the RITS-6 geometry have been undertaken and previously published [16]. Both 2D and 3D simulations have been performed. Depending upon the ratio of the load impedance to the MITL flow impedance, a *retrapping wave* [17] can be generated and propagates backward towards the generator. In such a wave, the bound current is observed to rise sharply as flow current is converted to bound current due to the impedance mismatch between the MITL and diode impedances. Because it is an accepted principle that voltage calculations using the Mendel equation [5-7] are valid only under equilibrium current conditions, and because such conditions are violated when local currents such as the bound current change quickly, the previous simulations only predicted the voltage in the MITL upstream of the load, not the load voltage itself. In the ion diode experiments [14,15] mentioned above, the load voltage was in fact simulated. Since appreciable retrapping waves were generated in the ion diode experiments, it is deemed pertinent to mention the behavior of the load voltage in those experiments, as detailed further below.

Since considerable data already exists for the SMP diode used with the Lo-Z MITL [9-11], and since the necessity for a “systems analysis” is observed to be more evident with the Hi-Z MITL operation, we concentrate here on characterization of the SMP diode as operated with the Hi-Z MITL. Data comparisons with shots taken with the Lo-Z MITL will be discussed as appropriate, in order to illustrate the significantly different behavior of the SMP diode load when driven with the Hi-Z MITL. The remainder of this paper is organized as follows:

- 1) Section II: experimental geometry and diagnostics are discussed. The arrayed PIN diode set is discussed, from which the inferred determination of the electron beam angle on the converter as a function of time was developed [13]. This technique makes use of the conventional  $cIV^x$  ‘Radiographic’ radiation scaling [18] (where  $x \sim 2.2$ ) for the PIN diode on the radiation axis.

In analyzing the Hi-Z MITL shots, it was noticed that the electron angles inferred from the  $cIV^x$  scaling differed from that of the same diode geometry operated with the Lo-Z MITL. Further analysis revealed that the  $cIV^x$  scaling begins to break down for voltages above 8 MV, and cubic scaling is required to recover accurate angle tracking. Details of this change are discussed in this section.

- 2) Section III: diode voltage estimation is critical to derivation of the various impedances introduced above (diode, total, parallel). At the same time, the estimation procedure is complicated by the behavior of the Hi-Z MITL with the SMP diode in place. Specifically, the Mendel theory as a method of calculating the MITL voltage had validity only when the total and bound MITL currents that contribute to the voltage calculation remain relatively constant. But the observed current waveforms, even for those monitors located far from the load (Section II), show a bound (inner conductor) current with a large *retrapping* wave that indicates at least initial coupling to an undermatched load, that is, a diode load impedance that is relatively small compared to the flow impedance of the MITL. Special techniques are developed in this section to estimate the corrected diode voltage, and intercomparisons with the diagnostic data are shown to result in a reasonably accurate self-consistent estimate for the diode voltage on a given Hi-Z MITL shot.
- 3) Section IV: MITL currents upstream of the diode load are the subject of Section III. In this section, currents in the diode region are described and compared to analogous currents observed in Lo-Z MITL shots. Unlike the Lo-Z MITL shot behavior, the load current is often observed to *decrease* instead of *increase* with time, even as the total current is steady or rising. This could be caused by *knob emission*, i.e. the generation of current from the circular field shaper upstream of the diode load that could occur due to the increased voltage stress that accompanies Hi-Z MITL shots. It could be argued that this is the reason for the decrease in the load current observed on many Hi-MITL shots. That is, there could be a transfer of diode current to sheath current implied by knob emission. The operative question to be addressed is not so much whether knob emission occurs, but whether any of the sheath current so created migrates to the diode load and adds to the load current that is presumed to be the source of the radiation dose. It will be argued in the data analysis in Sections IV and V that the  $I_L$  current (defined in Section II) current is the source of the radiation dose, i.e. no additional current from the presumed knob emission contributes to radiation dose.
- 4) Section V. By developing the concept of the three impedances discussed in the Introduction ( $Z_{\text{DIODE}}$ ,  $Z_{\text{TOTAL}}$ , and  $Z_{\text{PARALLEL}}$ ), it is shown that the decrease in load current can be explained as a natural outcome of the tendency of the IVA driver to deliver a current level consistent

with the flow impedance of the MITL in use. That is, the total available current is fixed, and if the diode load requires a current level that is inconsistent with this fixed current, then changes to the load current can and must occur. Note that this is a mathematical statement, as the causation mechanism is not discussed.

- 5) Section VI. The variation in performance with changes to the A-K gap for a fixed cathode diameter (17 mm in this case) is investigated, and compared to a similar A-K gap variation undertaken with the Lo-Z MITL. It is shown that variations in diode current, dose-rate, and diode voltage are significantly more compressed than in the Lo-Z MITL case. The A-K gap is chosen by the experimenter and is generally considered as an independent variable. This analysis implies that its independence is constrained in the case of the Hi-Z MITL.
- 6) Summary and Conclusions are left to Section VII.

## II. Description of RITS hardware, experiment geometry, and diagnostics

An overall simplified schematic diagram of the RITS-6 downstream MITL and load region is shown in Fig. 3. The inner MITL (gray) is connected to the IVA, out of view to the left. The outer MITL is expanded into a much larger chamber that contains the inner MITL field shaper and load region. The large chamber shown, known as the ‘dustbin’, is fielded in several sizes, enabling a variation in voltage stress between the inner and outer MITLs. Near the point where the dustbin is attached to the outer MITL, the inner MITL transitions to a conical structure (‘cone’), and then to the field shaper, or ‘knob’. The function of the knob is to divert the MITL flow away from the A-K region, because the quality of the electron flow has been regarded as not contributing to the minimization of the SMP spot size. (The discussion around Figs. 1a-c indicates that the diverted flow actually returns to the diode region during the power pulse.) The cathode is fielded on the downstream end of the knob, opposite the anode/converter. The red circle indicates that part of the drawing that is depicted in greater data, in Fig. 4. The red ‘Xs’ indicate the general position of Bdot current monitors that track the current flow towards the A-K gap. At the position marked ‘G’, just before the outer MITL is attached to the dustbin, are a set of 4 equally spaced Bdots in azimuth on both the inner and outer conductors from which average currents can be determined in both cases. From this location, the voltage coming forward towards the A-K region can be calculated using the modified theory of Miller and Mendel [6,7], as mentioned already. The form of the Mendel Equation used for this paper is given by an expression from Reference 6:

$$2) \quad V = Z_0(I_a^2 - I_c^2)^{1/2} - [(gmc^2/2e) * (I_a^2 - I_c^2)/I_c^2]$$

where  $I_a$  denotes the total current measured at a particular point in the MITL,  $I_c$  denotes the bound current at the same location,  $Z_0$  is the MITL vacuum impedance of the MITL, and  $g$  is a parameter of order 1. (If  $g$  is set = 1, the original Mendel equation is recovered.) The value of  $g$  is determined from particle-in-cell (PIC) simulations, and for an output voltage of  $\sim 8$  MV,  $g$  is determined to be  $\sim 0.8$ . Accordingly, this value of  $g$  is assumed for the duration of this paper. In practical terms, the difference between a  $g$  value of 1 and 0.8 amounts to  $\sim 0.2$  MV difference in the calculated voltage.

In addition to the inner and outer Bdots at position G shown in Fig. 3, there are two other positions in the MITL in which there are inner and outer Bdots at the same  $z$ -location, positions E and F, located upstream (to the left) of Position G. The Mendel formula can be used at those locations as well. These locations are out of field of view in Fig. 3 (to the left). The method of calculation of the corrected diode voltage is the same as discussed in previous RITS papers [9-11], i.e. the corrected voltage (hereafter referred to as  $V_{\text{CORR}}$ ) is calculated by inductively correcting the voltage at an upstream point where the voltage is determined from the Mendel formula:

$$(3) \quad V_{\text{corr}} = V_{\text{MITL}} - L_{\text{dustbin}} d[I_{\text{diode}}]/dt$$

where  $L_{\text{dustbin}}$  is the estimated lumped-circuit inductance of the dustbin chamber. To determine the value of  $I_{\text{diode}}$ , we refer to the other three ‘Xs’ indicated in Figure 2. The first X, located on the inner conductor near where the cone joins the field shaper, indicates where 4 equally spaced Bdots measure the feed (bound) current approaching the field shaper, a current referred to as  $I_{\text{UP}}$ , since the location is upstream of the diode. The second X, located on the downstream side of the field shaper, denotes where 4 Bdots are located at 6.35 cm radius from the diode axis. These Bdots measure the current flowing through the cathode, and possibly through a limited region of possible faceplate emission. This current is called  $I_L$ , where  $L$  stands for load current. It should be pointed out here that while Eq. 3 gives a mathematical prescription for calculating  $V_{\text{CORR}}$ , the formula contains several assumptions that may not be correct for the entire power pulse.  $V_{\text{MITL}}$ , for instance, is time-shifted to the diode position, typically by 7 ns, to approximately account for the transit time from the MITL position to the diode load. Voltages and currents at any point in a MITL (or conventional transmission line, for that matter) consist of a forward-going and return wave added together. In the lumped-circuit model described by Eq. 3, simply time-shifting a calculated voltage forward in time is likely to result in different return waveforms for the two respective axial positions. And  $V_{\text{MITL}}$  itself is determined from the currents (through Eq. 1), which are assumed to be accurate at any time during the power pulse. However, as the discussion below will illustrate,  $V_{\text{CORR}}$  as given by Eq. 3 appears to be a reasonably accurate estimate, on the average, of the

diode voltage. And, consistent with the conclusions of Sections IV and V,  $I_{\text{DIODE}}$  is considered to be the  $I_L$  current waveform.

As already mentioned in Section I, Eq. 2 is considered valid only when the total and bound currents ( $I_a$  and  $I_c$ ) that contribute to the MITL voltage calculation are relatively constant. There are two circumstances when this condition is violated: a) impedance collapse at the diode prior to the end of the power pulse; and b) coupling to a (at least initially) undermatched diode load, i.e. a load with a low diode impedance compared to the MITL impedance (the notion of “low” will be clarified later). In either case, a retrapping wave propagates back towards the IVA, and is measured on all current monitors. The retrapping wave occurs primarily on the bound current waveform, although a lesser version is observed on the total current waveform. Before the retrapping wave arrives, the magnitude of the bound current is typically  $\sim 1/3$  of the total current magnitude. With the retrapping wave arrival, the bound current level increases with steep slope to as much as 80% of the total current. The result is that a modification to Eq. 2 must be used. Its derivation and validation are the subject of Section III.

The final X on the right side of Fig. 3 marks the position of 4 Bdots located on the back vacuum wall at 11 cm radius off the diode axis. The current measured here is called  $I_A$ , where A stands for the anode side. This is the current monitor location referred to in the Introduction, where after a time lag, the total current measured in the upstream MITL (typically at the Position G) is observed to arrive in substantially the same magnitude and waveshape. This is the reason for the earlier statement that  $Z_{\text{TOTAL}}$  can be defined using either the upstream total current at Position G, or the current measured (after the time lag) at the  $I_A$  position.

On a typical RITS SMP shot taken using the Lo-Z MITL [9-11],  $I_{\text{UP}}$  tracks below the value of  $I_{\text{BEAM}}$  until near the end of the power pulse.  $I_L$  is always less than the value of  $I_A$ . This is a clear indication that there is current flowing in the diode region outside of the A-K gap. The most likely source of this current is the initially diverted MITL flow, which is drawn towards the A-K gap once the diode current rises. The dustbin depicted in Fig. 3 is the larger of two dustbins that were fielded in the RITS SMP experiments, with an estimated inductance of 330 nano-henrys. The value of  $L$ , however, contributes only as a second order effect.

In the case of the Hi-Z MITL shots discussed in this paper, on many shots  $I_{\text{UP}}$  exceeds  $I_L$  at some point in the power pulse. One reason for this is that on many shots, the  $I_L$  waveform decreases from an early peak. Since  $I_{\text{UP}}$  gives a measure of the bound current upstream of the knob and  $I_L$  location, if the magnitude of

$I_{UP}$  exceeds  $I_L$ , the clear implication is that bound current is being converted to sheath current, i.e. current is being emitted from the knob. This is what is referred to as knob emission.

A close-up schematic view of the diode region is depicted in Fig. 4. The cathode at left is indicated to be partially hollow, and faces an anode that is considerably larger in diameter. For the ‘standard’ SMP geometry, a foil (usually of aluminum 10 microns in thickness) is suspended as a flat plane approximately 0.7 mm offset from the converter plate made of tantalum (Ta). The function of the foil was characterized in earlier SMP experiments at the Atomic Weapons Establishment (AWE) [19] as helping to mitigate impedance reduction due to plasmas evolving from the Ta surface. To the right of the Ta converter is additional aluminum in the form of circular plates (not shown) that act as a beam stop. The initial electron beam approaches the anode in a non-pinchd manner. Then the rising current beam current deposits enough energy on the anode to heat and liberate ions from the anode. The source for these ions can be either monolayer contaminants on the surface that become ionized, or entrained ions in the atomic lattice of the anode. This occurs after the anode temperature has risen to some elevated value. Prior research [20] has suggested a threshold temperature of about 400° C as a thermal release point. These ions then counter-stream towards the cathode, and their presence helps neutralize the charge imbalance in the anode-cathode (A-K) gap. This in turn allows the electron beam to progress to a tight focus on the anode axis [21]. Simulations of current behavior in the RITS SMP diode using the hybrid particle-in-cell (PIC) fluid code LSP [22] confirm the formation of a tight beam pinch on the anode, occurring after about 10 nsec [23].

A comprehensive diagnostic set was fielded on the Lo-Z experiments on RITS-6, and is discussed in detail previously [9-11]. One diagnostic important for the analysis in this paper will be mentioned here. It is a set of three dose-rate monitors, P-I-N diodes mounted both unshielded and in shielded collimators, and fielded with accompanying TLDs mounted in proximity, allowing for absolute calibration of dose-rate. A schematic drawing of the PIN diode array set as fielded is shown in Fig. 5. In this drawing, the labeling of the PIN diodes refers to the angle of observation with respect to the radiation source. Thus, the PIN located on the axial location with respect to the radiation source (0°), and located behind both a lead collimator and aluminum plate, is labeled PIN\_0. The PIN located at the 45° observation angle is labeled PIN\_45. In the 95° observation direction, there were two PINs fielded, one inside a tungsten collimator, and one fielded outside the same collimator. The PIN fielded inside the collimator is labeled PIN\_95, and the PIN fielded outside the collimator is labeled PIN\_95 (uncoll). This Figure also shows the materials located between the photon source and the PIN diodes. (In the case of both PIN\_0 and PIN\_45, the

aluminum end flange of the vacuum chamber, which is in both their fields of view, is not shown for clarity.)

By comparing the relative dose-rate output from the PIN diodes, the evolution in time of the angle at which the electron beam impinges on the anode (referred to as the pinch angle) can be inferred. The methodology by which this is done has been extensively discussed [9,10,13]. We give a brief summary of the earlier work here, because one outcome of the investigation of the hi-Z MITL coupling to the SMP diode load is that the earlier results require modification. After the previous work is summarized, we give an updating of the modifications required.

The dose-rate  $D[\dot{D}]$  produced by electron impingement on the converter of a radiographic diode (and in fact other diodes as well) has been traditionally approximated by the following power-law form:

$$(4) \quad D[\dot{D}] = cIV^x$$

where  $I$  = current in Amperes,  $V$  = electron energy in MeV, and  $c$  is a constant. The factor  $x$  (referred to as the  $x$ -factor) depends upon the electron beam angle of incidence, the details of the x-ray converter materials, and the angle of observation. The form of Eq. 4 is referred to generically as a Radiographer's Equation [18], and different forms have been developed by various researchers. The  $x$ -factor has up to now been assumed fixed. Operationally, dose-rate is normalized to total dose by comparison with the output of TLDs which accompany the dose-rate detector in close proximity. This means that any time-dependent variability of the  $x$ -factor is lost. In the time-dependent dose-rate modeling method developed in Reference 13, electrons comprising the RITS electron beam are posited to strike the RITS-6 converter package at both specific angles:  $0^\circ - 80^\circ$  in 10-degree increments, and specific energies: 1-12 MeV in 1 MeV increments. The ITS -CYLTRAN code (cylindrical symmetry) [24] is then used to calculate photon spectra for each combination of electron angle and energy. Photon spectra are extracted in the  $0-10^\circ$ ,  $40-50^\circ$ , and  $90-100^\circ$  polar angle bins (angle bins correlated with the three PIN locations). Mass attenuation/absorption coefficients are used to attenuate the spectra as appropriate for the intervening materials in each direction and calculate the dose-rate in  $\text{CaF}_2$  (TLD material) for each of the three PIN detectors. These 27 datasets (9 electron angles and 3 observation directions) are then fit to dose-rate equations of the form:

$$(5) \quad D[\dot{D}]_N(\text{krad} - \text{cm}^2/\text{s}/\text{A}) = c_N \times V(\text{MV})^{x-N}$$

which follows the form of Eq. 4. The " $c_N$ " and " $x_N$ " parameters for each detector direction ( $N = 0^\circ, 45^\circ, 95^\circ$ ) are listed in a Table listed in Reference 13. The fit assumes that  $D_N$  follows Eq. 4 for a large

range of electron energies and electron angles. The accuracy of this assumption varies with individual angles and observation directions. Eq. 5 then constitutes a “Radiographer’s equation” that is specific to the RITS experiments when Table 1 values are used. Since dose-rate is a measured quantity for a given shot, Eq. 5 can be solved for diode voltage, given  $c$  and  $x$  for a particular angle, and the electron current. For this calculation, it is assumed that a constant percentage of the IBEAM current (15%) is composed of ion current, so IBEAM is multiplied by 0.85 to estimate the electron current. This is consistent with previous assumptions about the level of ion current on a typical RITS SMP shot [9-11]. Voltage waveforms can be constructed for a group of assumed electron angles, and then overplotted with the corrected voltage for the shot. Matching the corrected voltage to the various electron angle contours then yields an estimate for the electron angle as a function of time.

In practice, the PIN diodes in the 45° and 95° directions appeared to be affected by scattered photons within the RITS test cell, whereas the 0°-PIN appeared to scale accurately with the ITS-CYLTRAN modeling. The axial field of view towards PIN\_0 and TLDs 1-4 (Fig. 5) is collimated by a small (3 cm-diameter) aperture in an otherwise large lead shield located approximately midway between the diode and PIN\_0, followed by a 2.5 cm-thick aluminum plate (in the later set of RITS shots) placed directly in front of the PIN. Evidently, this level of shielding from scattered photons is more successful compared to the other two directions. Comparison of the dose-rates measured by the PIN\_95 and PIN\_95 (uncoll) monitors show that while the waveshapes are almost identical, the uncollimated monitor gives approximately twice the amplitude as the collimated one. Since neither of the TLD sets associated with the 95° direction (see Fig. 5) are collimated, it is apparent that the TLDs in the 95° direction are exposed to both direct and scattered photons. This makes the dose that they measure higher than those predicted by the CYLTRAN modeling. The net effect of the scattered photons is that the PIN\_95 detector magnitude appears to scale as  $IV^{1.1}$  (compared to  $\sim IV^{1.3}$  as in the Reference 13 Table), and the PIN\_45 detector magnitude appears to scale as  $IV^{1.8}$  compared to  $\sim IV^{2.5}$  scaling in the same Table.

While the  $cIV^x$  power-law scaling is extensively used in the discussion of SMP shot taken with the Lo-Z MITL [9], in this paper it is superseded by an updated methodology of calculating the inferred angles. This updating is necessitated by the following observation: the estimated load voltage on most of the Hi-Z MITL shots discussed in this paper exceeds 11 MV, at least for some period of time. When the power-law scaling was initially attempted to process the Hi-Z MITL data, it was found that the inferred electron angles showed an increase of 10-20° for an SMP diode where the cathode diameter is 12.5 mm, and the A-K gap is 12 mm (hereafter referred to as “12.5-12”). This is the same diode as was used for many of the Lo-Z MITL shots. For the larger A-K gap shots, where the aspect ratio was kept at 1:1 (i.e. cathode

diameter the same as the A- K gap), this systematic upward trend in angles was also noted. Now it is possible that the angles could in fact be larger, for whatever reason. But we take the position here that the electron angle for all 1:1 aspect ratio SMP diodes should remain approximately the same, at about 30° for at least an initial angle estimate. This is consistent with angle results or estimates from previous researchers [18, 25, 26]. It is thus important to find the reason for the indicated 10-20° increase in electron angle implied by the use of the power-law scaling to estimate the electron angle in the case the higher voltage Hi-Z MITL shots.

The cause for the discrepancy is found to lie in the use of the simple power-law form (Eq. 4). The procedure for using ITS simulations to construct the power-law scaling is discussed in Reference 13. In the discussion below Eq. 4 above, electrons are posited to strike the Ta converter package at specific energies and at specific angles. The results are then fit to  $cIV^x$  power-law scaling as shown in Fig. 6a. Also included are the  $c$  and  $x$  values associated with the 0° direction. Each of the dots is thus a separate ITS calculation. It can be seen that the fit of the curves to the data points is quite good for electron energies at or below 8 MeV (the peak energy encountered from the Lo-Z MITL shots), but deviate above this value. The deviation becomes quite noticeable at 11-12 MeV. The solution to this problem is to replace the  $cIV^x$  scaling by a scaling in cubic form:

$$(6) \quad \mathbf{D[\dot{d}ot]} = \mathbf{c1IV} + \mathbf{c2IV^2} + \mathbf{Ic3V^3}$$

where the coefficients for the linear, squared, and cubic terms are listed in Fig. 6b. It can be seen that the polarity for the three coefficients is (respectively) negative, positive, and negative (except for the first two elements). For energies typical of the Lo-Z MITL shots, the squared term is still dominant, but for the higher Hi-Z MITL voltages, the cubic term becomes more important. Using this cubic fit, it can be seen that now the fit to the ITS data points is extremely good.

We can compare the differences between use of Eqs. 4 and 6 (power-law vs cubic scaling) by examining the inferred angles for a shot discussed more extensively later in the paper, Shot 1861. This Shot featured a 17-mm cathode diameter and a 17-mm A-K gap (“17-17”). The inferred angles for 1861 using the power-law fit are plotted in Fig. 7a, and using the cubic scaling in Fig. 7b. It is observed that during the peak of the radiation dose-rate (~2.36  $\mu$ s), the inferred angle using the power-law scaling is 40°, as compared to an expected 30° as would be observed with the Lo-Z MITL shots. Using the cubic scaling (Fig. 7b), the inferred angle is close to 30°, then increases to 40° after peak power. This then illustrates the tendency of the cubic scaling to render an inferred angle more consistent with the Lo-Z MITL data.

The deviation between Eqs. 4 and 6 become evident above the 8 MV level (Figs. 6a and 6b). To check that the inferred angles obtained with the Lo-Z MITL experiments [9,13] remains unaffected, we compare the inferred beam angle obtained using the power-law vs the cubic for a shot taken with the Lo-Z MITL, Shot 1908, with an output voltage peak of about 8 MV. Data for this shot are shown in Fig. 8. The dose-rate in the axial direction is shown along with inferred angles using cubic scaling ( $\text{angle}(t)$ ) and power-law scaling ( $\text{angle}IV^x$ ). (The format of the angle data is obtained using interpolation.). The behavior of the angles is seen to be almost identical.

There are two implications for the use of a cubic fit, as compared to the power-law fit for the angles analysis for the Lo-Z MITL shots [9,13]. The first is that, unlike the power-law, the cubic scaling (Eq. 6) cannot be readily solved to determine the voltage. This is not a problem for the Hi-Z MITL analysis discussed in this paper, since we have determined a methodology to estimate the diode voltage independent of the dose-rate measurements (Section III). The second implication is that the assumption of a factor two scaling of the PIN\_95 dose-rate monitor that was used in the case of the Lo-Z MITL shots to establish a quantitative comparison with the axial dose-rate cannot be used here. This factor, the difference in size between the peak of PIN\_95 vs the PIN\_95 (uncoll) monitors, was exceeded in the case of the Hi-Z shots, reaching as high as 2.78 on some shots. This may be due to the enhanced presence of reflected photons in the RITS test cell with the higher-voltage Hi-Z MITL shots. This is why we discuss only the behavior of the axial dose-rate PIN (PIN\_0) in this paper. Note here that the angle contours plotted using the cubic scaling (cubic\_0 and so forth) are calculated using both the estimated diode voltage and the assumed radiation current  $I_L$  (multiplied by 0.85). Yet in many of the plots like Fig. 7b that are derived for this paper, the shape fit of the axial dose-rate matches the cubic scaling calculations, at least for individual angles and for some period of time during the power pulse.

It must be stressed here that the degree to which the simple power-law must be replaced by a cubic fit to obtain consistent results varies for any given experiment in general, and is affected for instance by the geometry of the converter package, thickness of the tantalum, and so forth. It is also noted here that for general matching of the voltage and current scaling to the axial dose-rate waveform used later in this paper, the power-law scaling is still used, as the  $cIV^x$  waveshape so generated is accurate enough to compare with the various dose-rate monitor signals. It is only when more precise indicators such as electron angles to the converter are required that the cubic scaling is important.

### III. Procedure for estimating diode voltage in Hi-Z MITL shots.

The schematic drawing in Fig. 9 illustrates the difference in dimensions between the Hi-Z and Lo-Z MITLS as fielded on RITS-6. The center conductor used in the Lo-Z MITL results in a vacuum impedance of 51.3 ohms, with an estimated flow impedance of 40 ohms. This conductor is depicted in the figure as the larger-diameter center conductor and outlined with the heavier dashed line. The lighter dotted line depicts the Hi-Z MITL, with a vacuum impedance of 102.8 ohms, and with an estimated flow impedance of 80 ohms. One motivating factor for use of the Hi-Z MITL is that since the flow impedance is approximately doubled, the output voltage should also scale similarly, and thus the output voltage can be expected to exceed that possible with the Lo-Z MITL.

As previously mentioned, the SMP shots taken with the Hi-Z MITL resulted in the presence of a strong retrapping wave on all shots taken, regardless of cathode diameter or A-K gap, indicating coupling to a relatively undermatched load impedance. The magnitude of the retrapping wave is demonstrated by comparing upstream total and bound MITL currents for two shots in which the same diode configuration was fielded, the 12.5-12 configuration previously introduced. One shot (1977) used the Lo-Z MITL, and the other (1884) was taken with the Hi-Z MITL. Total and bound waveforms are shown for the two shots in Fig. 10. The currents are measured at location E, which is well to the left of the monitors shown in Fig. 3, so as to maximize the time between the forward-going wave and any retrapping wave. (The E monitors are 4.27 meters or about 19 nsec removed (forward direction) from the IBEAM location.) As can be seen, both the total and bound currents for the Lo-Z configuration exceed those observed for the Hi-Z case. This is consistent with the higher MITL impedance of the Hi-Z configuration. But the most notable difference in the two shots is the behavior of the bound current. In the Lo-Z case (1977), the bound waveform remains roughly constant through the entire plot, indicating the absence of any retrapping wave during the timescale shown. By contrast, the Hi-Z bound current (1884) features a large retrapping wave, which arrives when the power pulse at this location is approximately two-thirds complete, whose magnitude almost equals the total current in size by the end of the power pulse. It should also be noted that when the retrapping wave begins, the total current is observed to rise by approximately 20%. This is the signature of a premature impedance collapse at the diode, which also results in a retrapping wave. But it is observed that even for shots in which no premature impedance collapse occurs, a strong retrapping wave such as occurs here is observed.

The existence of such a strong retrapping wave complicates the estimation of the load voltage. The reason has to do with the scaling in the Mendel equation for MITL voltage calculation (Eq. 2). The first (and dominant) term is the difference of squares. For a configuration in which the bound current peak exceeds

say 70% of the total current, the result is that the size of the first term begins to drop significantly with time when the retrapping wave arrives. The calculated MITL voltage appears asymmetric in time, i.e. the fall occurs faster than the rise. This can be demonstrated by examining the results of another set of experiments which featured coupling to an undermatched load impedance. Figs. 11a and 11b show waveforms predicted by LSP modeling for an experiment where the forward-going MITL current was coupled to a self-magnetically insulated ion diode [14,15] operated in negative polarity on the HERMES III facility. In the case of HERMES, the flow impedance is an estimated 27 ohms, and the diode impedance is estimated (with the A-K gap selected) from the LSP simulation at 18 ohms. The result is a significant retrapping wave produced at the load comparable to that shown in Fig. 10 for Shot 1977, which is visible in the bound current  $I_C$  (RED) predicted at a location 2 meters upstream of the diode load, shown in Fig. 11a. The total current  $I_A$  is shown in BLACK. While the two curves are LSP-generated, the shapes and magnitudes are chosen to match the experimentally measured currents at 2 meters upstream of the diode as closely as possible.

The relation between the total and bound current is similar to that seen for Shot 1884 in Fig. 10. The simulation then predicts the load voltage, which is plotted in GREEN in Fig. 11b, and should be compared to the voltage in the MITL 2 meters away (BLACK) and labeled as  $V_s$ , at the same location as the currents depicted in Fig. 11a. The MITL voltage peaks at 16 MV, whereas the load voltage shows a reduced peak of 12.5 MV. (The two other voltage waveforms shown are from intermediate positions.) But what is equally if not more significant is the *shape* of the two voltages. The upstream MITL voltage appears asymmetric in time, that is, the fall is much shorter in time than the rise. By contrast, the load voltage  $V_{AK}$  appears much more symmetric in time. If anything, the fall appears slower than the rise. While the inductive correction to the MITL voltage (Eq. 3) will slightly slow the rise and retard the fall, its addition will not change an otherwise asymmetric voltage waveshape into a symmetric one, like  $V_{AK}$ . Therefore, adding an inductive correction to the upstream MITL voltage cannot lead to an accurate load voltage waveshape. The strength of the retrapping wave prevents this from happening. A different approach is required.

Various prior design studies [27,28] have suggested that IVA coupling to an undermatched load has benefits. The reason is that the retrapping wave converts electron flow current to bound cathode current, which is judged to increase the efficiency of the radiographic source and enlarge the operating space for the combined IVA and radiographic load. This is clearly observed to happen in the HERMES case, as the  $I_{FLOW}$  current drops very rapidly as the bound current  $I_C$  rises. In the case of the SMP diode load, this prediction relies on the premise that since the flow current is posited to be diverted from the load by the

field shaper (the knob), increasing the electrode current should raise the load current. That this diversion does not occur in the RITS-6 experiments beyond a short time using either the Lo-Z or Hi-Z MITL can be readily shown. Three waveforms are each shown in two Figures, 12a (Shot 1908, 12.5 - 12 diode, Lo-Z MITL), and 12b (Shot 1889, 17 mm cathode diameter with 13 mm A-K gap ('17-13'), Hi-Z MITL). The BLACK curve in each figure is the total current measured at Position G (See Fig. 3), the GREEN curve is the current measured at the  $I_A$  position on the back wall of the load region. The respective waveshapes of the current at location G and at  $I_A$  can be compared by time-shifting the total current waveform at Position G to the  $I_A$  location. The amount of timeshift is chosen by matching the initial current rise at each location, and amounts to  $\sim 10$  nsec. In the Lo-Z MITL case (Fig. 12a), the difference curve (RED) reaches a peak of approximately 90 kA, with a FWHM of  $\sim 20$  nsec. The timing of the difference peak is connected with Stage 2, and decreases to zero with the arrival of Stage 3.

In the Hi-Z MITL case, the difference curve is almost nonexistent, as the time-shifted G current and the  $I_A$  waveform are almost the same. That is, except for the time delay, all the total current measured at Position G arrives at the  $I_A$  position almost unaltered. Thus, in neither MITL case is the goal of the knob as a current diverter successful. Thus the premise of the design studies cited above is violated. Still, there is a useful equation discussed in one of the studies [28]. A formula is proposed which estimates the diode voltage, given the power coming forward. The formula in such an undermatched case is as follows:

$$(7) \quad V_{DIODE} = V_{MITL} \frac{1 + \frac{Z_{MITL}}{Z_{FLOW}}}{1 + Z_{MITL}/Z_{DIODE}}$$

where  $Z_{MITL}$  is the vacuum MITL impedance,  $Z_{FLOW}$  is the flow impedance,  $V_{MITL}$  is the upstream voltage, and  $Z_{DIODE}$  is the diode impedance. Eq. 7 can be used to give an estimate for the load voltage  $V_{AK}$  in the case of the HERMES experiment above (Fig. 11b). With the HERMES vacuum impedance of 34 ohms, flow impedance of 27 ohms, and diode impedance at 18 ohms (from the LSP simulation), Eq. 7 predicts a load voltage of 12.5 MV. This equals what LSP predicts (GREEN), and gives confidence in the accuracy of Eq. 7.

We now describe the procedure for diode voltage estimation for the Hi-Z MITL SMP shots. This approach relies on the assumption that both the MITL currents and the dose-rate measurements given by the PINs are fundamental. The methodology is suggested by Fig 13, which shows upstream MITL currents and scaled PIN\_95 waveform from Shot 1861, a shot previously discussed and taken using a 17 mm-diameter cathode and 17 mm A-K gap (17-17). The dose-rate for this Shot in the axial direction was

analyzed using both the power-law and cubic scaling estimates and presented (respectively) in Figs. 7a and 7b. The total and bound currents from positions E and F are timeshifted forward so that their rise matches that of the  $I_L$  current (not shown), +18 ns and +15 ns for positions E and F, respectively. (For the calculation of  $V_{CORR}$  at Position G for the Lo-Z MITL shots, the G currents are typically time-shifted +10 ns.). Comparison with the timing for the PIN\_95 waveform indicates that (at this time-shift), the arrival of the retrapping wave at position E occurs more than halfway through the power pulse, i.e. after the point where PIN\_95 has peaked. Prior to this time, the bound current appears relatively constant in time. The bound current at position F, by comparison, arrives less than one-third of the way through the power pulse, and prior to that is slowly rising. The bound current at position G (not shown) does not exhibit any period of flat current.

Since the Mendel equation yields a fairly consistent value for the MITL voltage at position E before the retrapping wave arrival, we choose to use the voltage estimate at E ( $V$  at E), and time-shift this value to the location of IBEAM (the 18 ns value is typical). One anecdotal justification for this time-shift is that on the Lo-Z MITL experiments [9], in calculating the corrected voltage for several shots (including Shot 1908 already mentioned), inductively corrected voltage estimates were generated using all three upstream voltage estimates ( $V_{CORR\_E}$ ,  $V_{CORR\_F}$ , and  $V_{CORR\_G}$ , with suitable time-shift). All three calculations were found to be virtually identical. The remainder of the voltage waveform after the retrapping wave arrival at Position E (at 2.372  $\mu$ s in Fig. 10) is then truncated. The truncated  $V$  at E is inductively corrected using the differentiated  $I_L$  waveform, as is done with the Lo-Z shots. What then replaces the truncated voltage late in time is suggested by Figs. 14a-b. As mentioned in Section II, the empirical scaling of the PIN\_95 dose-rate using the power-law fit [9,13] is with an x-factor of 1.1. This means that the dose-rate in the 95° direction scales almost linearly in both current and voltage. The three PIN signals (PIN\_95, PIN\_45, and PIN\_0) are plotted and scaled to unity in a heuristically useful way in Fig. 14a. In this plot we discount the two sharp and short-lived spikes in the PIN\_95 signal in the middle of the radiation pulse. These are likely caused by sudden electron spikes to the anode structure in a manner not observable by the other two dose-rate monitors. The three waveforms have differing slopes on their rise that arise simply from the different x-factors in their power-law scaling, 1.1 for PIN\_95, 1.8 for PIN\_45, and 2.2 for PIN\_0. That is, the higher the x-factor, the narrower the pulse when scaled to unity.

In Fig. 14a, it is observed that both the PIN\_45 and PIN\_0 waveforms begin to fall after peak at about the same time ( $\sim 2.365 \mu$ s). This might be taken to mean that the load voltage has begun to fall, but the relatively constant value for PIN\_95 at the same time contradicts this interpretation. The reason then for

the fall in the PIN\_0 and PIN\_45 signals can be seen by referring back to Fig. 7b. At the time that the dose-rate\_0 in the Figure begins to fall, the angle of the electrons on the anode converter increases, from 30 to 40 degrees. This decreases the x-factor and hence the dose-rate, without the load voltage falling, which is consistent with the PIN\_95 waveform.

To construct the estimate for VCORR, the PIN\_95 signal is truncated for times  $\leq 2.372 \mu\text{s}$ , divided by the load current  $I_L$ , and scaled and spliced into the inductively corrected Voltage at E mentioned above, which was truncated at  $2.372 \mu\text{s}$ . The result is shown in Fig. 15a, where the composite VCORR waveform (BLACK and RED) is plotted with what VCORR would have been if the entire Voltage at E (i.e including the truncated part) (GREEN) had been used for the inductive correction. The composite waveform is observed to remain at higher voltage for a longer duration, similar to what is observed for the load voltage  $V_{AK}$  compared to the upstream MITL voltage  $V_5$  in the HERMES data shown in Fig. 11b. As a check, the composite VCORR waveform is raised to the 1.8 power (empirical scaling for PIN\_45) and plotted with the (scaled) PIN\_45 signal in Fig. 15b. The fit is seen to be quite good. This helps to validate the procedure described here to construct the candidate corrected load voltage waveform VCORR. As a further check, the load voltage can be estimated using Eq. 7 [28]. The voltage at the upstream MITL is estimated to be  $\sim 12 \text{ MV}$ , from the Mendel equation. With the known vacuum and flow impedances for RITS-6, the estimate for the diode voltage is then  $10.6 \text{ MV}$ . This compares favorably with the  $\sim 11.6 \text{ MV}$  value obtained from Figs. 17a. A similar analysis of the lone shot taken with a 20 mm-cathode and 20 mm A-K gap (1865) shows very similar behavior. Thus we have two Hi-Z shots where the electron angle to the converter is estimated to be in the  $30^\circ$  to  $40^\circ$ , and thus consistent with angles estimated for the Lo-Z MITL shots [9] taken with 1:1 aspect-ratio diode configurations.

We thus conclude that the method described here for approximating the diode voltage in the presence of a strong retrapping wave, which occurs on all the Hi-Z MITL shots, results in a credible estimate for the diode voltage. The voltage estimate can then be used to construct the three impedances discussed in the Introduction –  $Z_{\text{DIODE}}$ ,  $Z_{\text{TOTAL}}$ , and  $Z_{\text{PARALLEL}}$ . These impedances have heuristic value, as will be further explained in the sections below.

#### **IV. Behavior of diode-region currents. Comparison with Lo-Z MITL performance.**

The behavior difference of the upstream currents between the Lo-Z and Hi-Z MITL cases was illustrated in Fig. 10, as a way of introducing the discussion of diode voltage estimation on Hi-Z MITL Shots. The behavior of the diode currents ( $I_A$ ,  $I_L$ , – see Fig. 3) differs significantly between the Lo-Z and Hi-Z MITL shots. The respective  $I_A$  and  $I_L$  waveforms for the same two shots compared in Fig. 10 (1884 and 1977) is shown in Fig. 18. The shot currents are plotted so as to match their initial rises. In the case of Shot 1977 (Lo-Z MITL), the rise of the  $I_A$  and  $I_L$  is delayed relative to Shot 1884, and the two currents then separate relatively early in their rise. After that, the currents rise with the same slope, which means that the difference current ( $I_A - I_L$ ) remains approximately constant for the rest of the power pulse. The two currents rise sooner and with steeper slope in the case of Shot 1884, and rise together until very near the peak of their initial steep slope. Only then do the  $I_A$  and  $I_L$  currents separate, after which  $I_A$  rises at a faster rate than  $I_L$ . Thus, the difference current in this case rises steadily over time. Since the difference between  $I_A$  and  $I_L$  can be considered a rough measure of the sheath current, this suggests that with the Lo-Z MITL, sheath current remains constant to first order, while it rises during the power pulse in the case of the Hi-Z MITL. This point will be discussed further below. On Shot 1884, both  $I_A$  and  $I_L$  reach an inflection point, after which both currents rise relatively quickly. This last behavior illustrates the apparent impedance collapse on Shot 1884, as already mentioned.

The behavior of the diode currents is even more different from the Lo-Z MITL case for the 17 – 17 (and 20-20) shots. The three diode currents ( $I_A$ ,  $I_L$ ,  $I_{UP}$ ), the (scaled) axial dose-rate (PIN\_0), and the difference current ( $I_A - I_L$ ) for Shot 1861 (17-17, discussed above) is plotted in Figure 17a. As with Shot 1884, the difference current rises over time, but unlike Shot 1884, the  $I_L$  current does not just rise slowly, it actually *falls* with time. This is never seen with the Lo-Z MITL shots, where load current is observed to rise with time as the electrode plasmas approach each other, reducing the effective impedance. The cause is seen to be unrelated to the power coming forward, as  $I_A$  remains relatively constant during the same time period. The rising  $I_{UP}$  current then exceeds  $I_L$  after the latter begins to fall. This then is an example of indicated knob emission, as previously described. Since the use of the Hi-Z MITL raises voltage stress on the various diode-region components, and since anecdotal signs of such emission are observed (small arc-marks on the knob, for instance), evidence for knob emission exists. There would not appear to be an alternate explanation accounting for a fall in the  $I_L$  current with time.

It is instructive here to view the four individual signals making up the load current  $I_L$  average are shown for Shot 1861 in Fig. 21b. The individual currents making up  $I_L$  (or any such current average) are rarely plotted or noted in this paper, because such individual currents are not notable, that is, the signals usually vary little between the four waveforms. That is not the case for the four  $I_L$  signals. They vary both in

magnitude and in waveshape. The same is true for the two  $I_{UP}$  signals (not shown). The four individual  $I_A$  waveforms (not shown), by contrast, display similar waveshapes and vary by  $\pm 5\%$  in their magnitude. The  $I_L$  waveforms thus display rather puzzling behavior. One possible explanation would be that this is a sign of knob emission. The  $I_{UP}$  waveform is observed to exceed  $I_L$  even before the latter waveform has peaked and begun to fall.

The composite diode voltage for Shot 1861, constructed using the PIN\_95 waveform later in time, has already been shown (Fig. 15a). The empirically based  $IV^{1.8}$  scaling of the diode voltage using the IBEAM waveform was shown to be consistent with the PIN\_45 signal (Fig. 15b). Thus, the behavior of the dose-rate monitors is shown to be consistent with a fall in the diode *current*, not the *voltage*. We examine more carefully the behavior of the diode current in the next section.

### **V. Interdependence of the $Z_{DIODE}$ , $Z_{TOTAL}$ , and $Z_{PARALLEL}$ impedances: An illustration of IVA-Diode coupling. Re-labeling of $Z_{DIODE}$ as $Z_{LOAD}$ .**

In the Introduction, the impedances  $Z_{DIODE}$ ,  $Z_{TOTAL}$ , and  $Z_{PARALLEL}$  were introduced.  $Z_{DIODE}$  is defined as the corrected diode voltage divided by the current flowing through the diode and producing radiation generation.  $Z_{TOTAL}$  uses the total system current instead of the current flowing through the diode, and based upon the observed currents in the Hi-Z MITL (Fig. 12b), either the time-shifted total current at Position G or the  $I_A$  current can be used.  $Z_{PARALLEL}$  refers to the current flowing in the diode region, but not through the diode, and is defined using Eq. 1. Here we re-label the term  $Z_{DIODE}$  as  $Z_{LOAD}$ , since that impedance is defined using the current labeled  $I_L$ . The label  $Z_{TOTAL}$  remains the same.

We first discuss the impedance behavior of Shot 1861 (17-17), for which estimated diode voltage and  $I_L$  current were shown in Figs. 15a and 17a, respectively. Estimates for  $Z_{LOAD}$ ,  $Z_{TOTAL}$ , and  $Z_{PARALLEL}$  can then be constructed using these quantities as prescribed in the Introduction. The plots for  $Z_{LOAD}$ ,  $Z_{TOTAL}$ , and the MITL impedance at Position E ( $Z$  at E), the latter time-shifted to the diode location, are shown in Fig. 18a. In addition to these waveforms, a (scaled) PIN\_0 and  $Z_{PARALLEL}$  are added in Fig 18b. In Fig. 18a, after large early signal levels in both  $Z_{TOTAL}$  and  $Z_{DIODE}$  attributable to the small current levels early in the pulse,  $Z_{TOTAL}$  is seen to closely follow the (constant)  $Z$  at E waveform at approximately 80 ohms. This is consistent with the behavior seen in Fig. 2, where  $Z_{TOTAL}$  is roughly equal to the Lo-Z MITL flow impedance, whereas for the Hi-Z MITL shots, the flow impedance is 80 ohms. But it is the behavior of the  $Z_{LOAD}$  waveform that is most interesting here. After the initial high level, it levels off at approximately 90 ohms, then rises continuously to reach as high as 120 ohms. This behavior cannot be explained by any kind of electrode gap closure argument. Yet it is consistent with the behavior of all three dose-rate

monitors. It is as if the diode current, having risen very quickly along with  $I_A$ , is then forced to fall back to a lower level. At the same time,  $Z_{\text{PARALLEL}}$  (Fig. 18b) is seen to fall from a very high level (almost no flow current) to below 200 ohms at the end of the power pulse. The interpretation is that diode current is being converted into flow current, exactly the opposite process to that described in References 27 and 28. Note that this conversion occurs even as  $Z_{\text{TOTAL}}$  remains relatively constant.

Now it is not clear what the causal mechanism is here for the current behavior as described. But if one accepts the premise as plotted in Fig. 2, namely that the generator delivers a total current equal to its flow impedance, and if the  $V_{\text{CORR}}$  waveshape has the correct shape, then the behavior of  $Z_{\text{LOAD}}$  must follow as described. In addition, the ultimate impedance of the diode at  $\sim 120$  ohms meets the criterion stated in the earlier Lo-Z MITL paper [9] that the diode impedance should be at least 1.5 times the flow impedance of the MITL. The path by which the diode impedance reaches that point, however, is not clear from a causal standpoint.

To emphasize the difference in behavior of the various impedances in Figs. 18a and 18b from what is observed with the Lo-Z MITL, a similar study to that in Fig. 22b is presented in Fig. 23. The Lo-Z MITL shot chosen for comparison is Shot 1977, taken with a 12.5-12 configuration. Waveforms from this shot were already presented in Figs. 10 and 16. The analogous waveforms to Fig. 18b are plotted for Shot 1977 in Fig. 19. The exception is that in addition to the impedance  $Z$  at E, we include also the impedance  $Z$  at G, since corrected diode voltage in Shot 1977 was in fact calculated at the G position. The two impedances are observed to be almost identical. As in Fig. 19b, the impedances at E and G are timeshifted to the diode position to reflect their respective transit times (+11 ns from G, +18 ns from E). The 1977 waveforms are adjusted to start at the point where the respective currents at E begin for the two shots. Several differences are noted between the respective waveforms in Fig. 18b and Fig. 19. The 1977  $Z$  at G and  $Z_{\text{TOTAL}}$  curves approximately track the 40 ohm line, consistent with the flow impedance of the Lo-Z MITL. The diode impedance  $Z_{\text{LOAD}}$ , after large oscillations early in time (reflecting small current levels), becomes steady at an initial  $\sim 65$  ohms, then falling steadily due to electrode gap plasma closure. This is consistent with earlier studies of  $Z_{\text{LOAD}}$  behavior on RITS shots [9-11]. The biggest difference between the waveforms in Figs. 18b and 19, however, is with the  $Z_{\text{PARALLEL}}$  waveform. In Fig. 18b, as already noted,  $Z_{\text{PARALLEL}}$  falls steadily through the power pulse, reflecting the conversion of diode current to sheath current. In Shot 1977,  $Z_{\text{PARALLEL}}$  rises steadily, reflecting the opposite, i.e. sheath current is being converted to diode current.

The implications of the conversion of diode current to sheath current in HI-Z MITL shots cannot be overstated. To the extent that maximum dose is a desirable outcome for SMP shots, any reduction in diode current places a limit on achievable dose. This helps to explain why, as a group, the Hi-Z MITL shots did not yield as high a radiation dose (nor as small a spot size) as shots taken with the Lo-Z MITL in place. (The other reason is a reduction in Marx generator charge caused by indications of voltage-stress related local breakdowns.) We can gain more insight to the dynamics of current transfers between sheath and diode current by examining the behavior of the bound currents as the power comes forward towards the diode load. The bound currents comprise the currents flowing in the inner (cathode) MITL at locations E, F, and G, plus the  $I_{UP}$  (upstream of the knob) and  $I_L$  monitors (refer to Fig. 3). Waveforms from all five locations are plotted for the two respective shots (1861 and 1977) in Figs. 20a and 20b. It must be stressed that these signals are not time-shifted. In Shot 1861 (Fig.20a), the  $I_{UP}$  current rises after the currents at E, F, and G, but then quickly overtakes those currents as well as the  $I_L$  current, which rises slightly later. Later in the power pulse, after  $I_{UP}$  reaches its peak, the difference between  $I_{UP}$  and  $I_L$  increases as the latter current falls, as previously noted. The rapid rise of the  $I_{UP}$  current indicates a strong retrapping wave caused by the initially undermatched load. However, this bound current clearly decreases with time at the  $I_L$  location. The difference points to current converted to sheath current with time. By contrast, on Shot 1977 (Fig. 20b), the  $I_{UP}$  current rises but always remains well below the  $I_L$  current level after  $T \sim 2.29$   $\mu\text{sec}$ . This implies that sheath current flowing at the  $I_{UP}$  location is being converted to bound current. Both behaviors are captured by and consistent with the  $Z_{PARALLEL}$  waveforms in Figs. 18b and 19 respectively.

The insight into the relative behavior of the bound currents in the Hi-Z MITL shots compared to Lo-Z MITL (Fig. 20a vs 20b) can be extended by comparing the behavior of the sheath current in total as a function of axial position. The sheath current can be calculated easily at positions E, F, and G by simply subtracting the bound current from the total current at these positions. We can get an approximate value for the sheath current at the  $I_L$  position by considering a set of Bdot current monitors not previously mentioned. These are a set of three monitors located on the outer dustbin wall (see Fig. 3). These monitors typically indicated peak currents approximately comparable to the total currents at E, F, and G, and two of the sets were located near the axial location where the  $I_L$  monitors are located. The two signals are averaged together, then  $I_L$  (as a bound current) is subtracted from the result.

Two sets of sheath current plots are shown in Fig. 21a and 21b. They are for, respectively, a Hi-Z MITL shot (1861, 17-17, previously described), and a Lo-Z MITL shot (1908, 12.5-12, previously described). In the case of Shot 1861 (Fig. 21a), the sheath current at E shows a truncated pulse-width, as the strong retrapping wave arrives. The pulsewidths at F and G are even shorter, because the retrapping wave arrives

sooner at those locations. The retrapping wave begins of course at the load position, and the sheath current at  $I_L$  is reduced to almost zero. It then rises throughout the power pulse, indicating the conversion of diode current to sheath current. In the case of Shot 1908 (Fig. 21b), the sheath current at E is observed to be full-pulse, because the retrapping wave only approaches position E near the end of the power pulse. The sheath current decreases at positions F and G, and begins at the  $I_L$  position at approximately the same amount as at position G. It then falls during the remainder of the power pulse, indicating the conversion of sheath current to diode current, the opposite of what occurs in Shot 1861.

The behavior of the sheath current at IBEAM can be connected more explicitly to the decline in the IBEAM current for HI-Z MITL shots in the following manner. Recall from Fig. 3 that the  $I_A$  current monitors are located on the back wall of the anode region, and the  $I_L$  monitors are located near the base of (and off the axis) of the cathode base. The respective waveforms from  $I_A$  and  $I_L$  for the 17-17 Shot 1861 were shown in Fig. 17a. The two signals are observed to track each other upward until they diverge at  $\sim t = 2.34 \mu\text{s}$ , with  $I_A$  continuing to rise after that, and  $I_L$  falling in time. The difference of the two ( $I_A - I_L$ ) is also plotted in Fig. 17a. The sheath current at the  $I_L$  position, already shown in Fig. 21a, is compared with the ( $I_A - I_L$ ) waveform in Fig. 22. The waveshapes are observed to be virtually identical except near the signal peak. The difference there may be attributable to the fact that neither of the Bdot sets out at the dustbin wall is exactly in the same axial position as  $I_L$ , and therefore the sheath current is an approximate value. Thus, the fall in the  $I_L$  current is shown to be directly correlated with the rise in the sheath current with time, which validates the transfer of diode to sheath current.

Not only does the sheath current behavior vary dramatically between the Lo-Z MITL and Hi-Z MITL cases, but the current to the load starts sooner in the case of the Hi-Z MITL shots. This can be seen by referring back to Figs. 12a and 12b. Because of the initial shunting of the flow current to the outer dustbin wall seen in the low-Z MITL shot (1908 – Fig. 12a), there is a time lag of approximately 20 ns before the sheath current arrives fully in proximity to the load region ( $I_A$ ). In the Hi-Z MITL case, the only time lag between positions G and  $I_A$  is the propagation time. It can then be asked if this difference in sheath current behavior leads to any differences in diode behavior between the two MITL impedances. For instance, does the radiation pulse also start earlier? We can investigate this by comparing two shots taken with the same diode configuration (12.5-12), and with the Lo-Z MITL (1908) compared to the Hi-Z MITL (1884). The  $I_L$  waveforms as well as the (scaled) PIN\_0 monitor signals for the two shots are compared in Fig. 23a. The 1884\_  $I_L$  is observed to rise without the slight delay seen in 1908\_  $I_L$ . The 1884\_PIN\_0 signal also rises sooner, by about the same amount in time, indicating the onset of radiation tracks the earlier  $I_L$  onset. The 1884\_PIN\_0 dose-rate is seen to be almost as large as the (later) peak in

1908\_PIN\_0. The 1884 pulse duration is shorter than for Shot 1908, due to the premature impedance collapse seen on Shot 1884. We can compare more precisely the dose-rates by calculating the absolute dose-rate in units of krad-cm<sup>2</sup>/amp for the two shots. The comparison is shown in Fig. 23b. The dose-rate *per unit current* for Shot 1884 is observed to exceed that of Shot 1908 early in time before the impedance collapses in the case of Shot 1884. Put another way, the diode in Shot 1884 is more efficient at producing dose than in Shot 1908. That is probably because the diode voltage V<sub>CORR</sub> in Shot 1884 is higher early in the pulse than for Shot 1908. The respective estimated diode voltages for the two shots are shown in Fig. 24a. This suggests but does not confirm that the I<sub>L</sub> waveform for Shot 1884 accurately portrays the radiation current. But there is another way to check on the validity of the Hi-Z MITL I<sub>L</sub> current as the true source of the radiation dose.

In the previous study of electron angle change as a function of time [13], a modeling study utilizing ITS simulations resulted in a power-law fit to the dose-rates for a given SMP shot previously stated as Eq. 5:

$$5) \quad \mathbf{D\_N(krad - cm^2/s/A) = c\_N \times V(MV)^{x-N}}$$

where c is the coefficient, x is the power-law factor (X-factor), and N indicates a direction of observation of the radiation. For the present study, the left-side of this equation is calculated using the PIN\_0 monitor, the TLD in close-proximity, and the measured I<sub>L</sub> current (minus the 15% presumed ion current). The right-side is calculated using the estimated load voltage V<sub>CORR</sub>, and the c and x values are determined for a particular electron angle by using Table 1 of Reference 13. We have previously indicated that while a cubic fit to the ITS data is required to infer more precisely the electron angle, for more general purposes of shot scaling and comparison, a power-law fit has adequate precision for the present purpose.

We make use of Eq. 8 in the following manner: consider both Shot 1884 and 1908, and form the ratio of the left and right sides of Eq. 8. For this purpose, the c coefficient drops out. Since the electron angles have been shown to be roughly equivalent for both Shots 1884 and 1908, a fixed angle of 30° is assumed for both shots. From Table 1 [13], x = 2.34. The rest of the ratio is obtained from the respective I<sub>L</sub> and V<sub>CORR</sub> for both shots. The final assumption made is that both the radiation magnitude and the I<sub>L</sub> current are assumed to be accurate for Shot 1908, since prior analysis [9-11] have indicated that this is so. Then under these assumptions, the ratio of the left-side should be approximately equal to that of the right-side.

The left-side and right-side ratios for Shot 1884 and 1908 are plotted in Fig. 24b, along with a (scaled) 1884\_I<sub>L</sub> signal for timing comparison. For the majority of the radiation peak (2.26 to 2.28 μs), the ratios

are observed to be approximately equal in size. This validates the accuracy of the 1884\_  $I_L$  current as the radiation source. In addition, since the ratio of the  $V_{CORR}$  magnitudes is raised to the 2.34 power, any significant deviation of the estimated voltage from the true voltage would render the right-hand side different from the left. This then validates the process previously discussed in which the estimate for  $V_{CORR}$  is derived.

One last comparison between Shots 1884 and 1908 is instructive. Similar to the comparison of impedance behavior between a Hi-Z MITL shot (1861) and Lo-Z MITL shot (1977) in Figs. 18b and 19 (respectively), we investigate the relative behaviors of  $Z_{TOTAL}$  and  $Z_{LOAD}$  for Shots 1884 and 1908. Comparisons of  $Z_{TOTAL}$  are shown in Fig. 25a, and of  $Z_{LOAD}$  in Fig. 25b. Also plotted in Fig. 25a are (respectively) the MITL impedance  $Z$  at position G for Shot 1908, and position E for Shot 1884. Those positions are chosen to sample the MITL  $Z$  because the corrected voltage was calculated for these shots at those respective locations. The MITL  $Z$  is observed to follow approximately the 80 ohm curve for Shot 1884, and the 40 ohm curve for Shot 1908, reflecting the flow impedances for the Hi-Z MITL and Lo-Z MITL shots respectively. The  $Z_{TOTAL}$  waveform for Shot 1908 tracks approximately along the  $Z$  at G curve through the middle of the power pulse, whereas  $Z_{TOTAL}$  for Shot 1884 approximates the  $Z$  at E curve early in the power pulse, then declines steadily to  $\sim 70$  ohms before the impedance collapses.

But it is the behavior of the respective  $Z_{LOAD}$ s that shows the most striking behavior (Fig. 25b). For Shot 1908,  $Z_{LOAD}$  begins initially at  $\sim 65$ -70 ohms, then falls steadily to about 40 ohms at the end of the power pulse. This reflects the normally observed reduction in the effective A-K gap in a high-power diode due to the convergence of the electrode plasmas. On Shot 1884, however,  $Z_{LOAD}$  a) averages  $\sim 90$  ohms through the (shortened) power pulse, and b) does NOT decline with time. Recall that the exact same diode geometry and A-K gap is employed on both shots. This implies that a) the effective SMP diode impedance (and for probably other types of diodes as well) *depends upon the flow impedance of the driving IVA*; and b) either the electrode plasmas in the diode do not converge during the power pulse, an unlikely outcome, or the convergence is masked by the behavior of  $I_L$ . That is, since 1884\_  $I_L$  rises fairly slowly (see Fig. 18), then  $Z_{LOAD}$  which is calculated by dividing the estimated diode voltage by IBEAM appears to hold steady. A streak camera diagnostic, fielded on the Lo-Z MITL shots [9], could address this question, but that diagnostic was not fielded on Hi-Z MITL shots. The cause of the premature impedance collapse on Shot 1884, and indeed all the shots with A-K gaps smaller than 17 mm, is not determined in this paper. One of the standard arguments for such a collapse, that of converging electrode plasmas, cannot be determined here, since the  $Z_{LOAD}$  waveform shows no evidence for a declining effective A-K gap.

**VI. Variation in load current with changes in A-K gap: 17 mm HI-Z MITL shots.** The behavior of the SMP diode with variations in A-K gap using the Lo-Z MITL (holding the cathode diameter fixed) has been previously explored [9], using shots at the 4.5 MV level and with a cathode diameter of 7 mm. For comparison with the Hi-Z MITL in place, we look at a set of shots taken with the 17 mm cathode, and A-K gaps of 17, 15, and 13 mm. Two shots were also taken with 19 mm A-K gap, but both shots suffered immediate fast current rise and impedance collapse, and are not discussed here. It must be pointed out here that by far the most shots taken with the 17 mm-cathode size were taken with an A-K gap of 17 mm (17-17). A shot with the 17 mm A-K gap (17-17) has already been extensively investigated above (1861). In this section, Shot 1861 will be compared with one of the two shots taken at 15 mm A-K gap (1890: 17-15), and the lone shot taken with a 13 mm A-K gap (1889: 17-13). A comparison of the  $I_L$  currents for the three respective shots is shown in Fig. 26a, which should be compared with  $I_L$  currents from a previous 4.5 MV shot series taken using the Lo-Z MITL [9] (Fig. 26b). The  $I_L$  currents in the 4.5 MV series diverge in magnitude relatively early in their rise, and then proceed on different load lines. By contrast, the three  $I_L$ s in Fig. 27a all rise together until nearly the first local maximum. Only then do they vary in magnitude, and the variation is accomplished by *declines* in both the 15 mm and 17 mm A-K gap shots (1861 and 1890). As mentioned before, these declines are not caused by decreases in the IVA driving current. The three plotted waveforms at the bottom of Fig. 26a are the result of subtracting the  $I_L$  current from the  $I_A$  current for the respective shots, i.e. they indicate the sheath current in the load region for the three shots. These waveforms will be discussed further below.

The behavior of both sets of waveforms in Fig. 26a contrasts significantly from the current behavior in the Lo-Z MITL 4.5 MV shots, and reinforces the observation made in the previous section that in the Hi-Z MITL case, the “ultimate” diode impedance only occurs later in the pulse, after the relative amounts of diode and flow currents have adjusted. The  $I_A$  waveforms for the same 3 shots (not shown) also only show variation after reaching a first local maximum, but none of the  $I_A$  waveforms show actual declines after reaching the first local maximum. A subset of three of the Lo-Z MITL shots depicted in Fig. 26b is chosen (for clarity), and are plotted along with their respective ( $I_A - I_L$ ) waveforms in Fig. 27. The shots shown are: Shot 1537, with 7 mm cathode diameter and 7 mm A-K gap (‘7-7’), Shot 1541 (‘7-6’), and Shot 1549 (‘7-4’). Besides the relatively early separation of the IBEAM signals into separate load lines, the amount of sheath current is observed to vary depending upon the diode configuration. The lowest sheath current is associated with the smallest A-K gap, and rises as the A-K gap is increased. This is quite different behavior from the ( $I_A - I_L$ ) waveforms plotted for the 17 mm Hi-Z MITL shots, shown in Fig. 26a. In those shots, the amount of local sheath current remained the same as the A\_K gap was varied.

In the case of the 4.5 MV shots with the Lo-Z MITL, the dose and dose-rate of the axial PIN\_0 (not shown) showed clear increases as the A-K gap was increased. The PIN\_0 dose-rate waveforms for the three HI-Z MITL shots in Fig. 26a are shown in Fig. 28a. It is observed that the peak dose-rate for Shots 1861 and 1890 are almost the same, with the 1889 peak being somewhat lower. However, the measured total dose@ 1meter (from TLDs) for Shot 1889 (17-13) is actually higher than that for Shot 1890 (17-15). The range of dose for the 17-17 shots (which includes 1861) showed a large variation ( $\pm 20\%$ ) around an average of 435 rads, compared to 380 Rads for Shot 1890 and 406 rads for Shot 1889. This is as compared to a 50% increase in dose for an equivalent range of A-K gap variation in the 4.5 MV shots series taken with the Lo-Z MITL (9). It might be noted that the variation in load voltage in the three Hi-Z MITL shots (Fig. 28b) is quite small. The variations in dose come from two effects: 1) as the A-K gap is reduced, the angle of electron strikes to the converter increases. Using techniques described in Reference 9 to infer the electron strike angle, we conclude that on the 17-17 shots, this angle varied between 30 and 40 degrees. The angle steepens to 50 degrees for the 17-15 shot, and up to 60 degrees for the 17-13 shot. As the angle increases, the dose-rate drops; and 2) as Fig. 26a shows, as the A-K gap is reduced, IBEAM increases and the reduction in current later in the pulses is almost eliminated as the gap is closed to 13 mm. The net result is a compression in the dose-rate and total dose seen in these experiments. Overall, it can be said that the range of diode behavior with variation in A-K gap is compressed compared to that seen with the Lo-Z MITL in place. That is, the variation in the A-K gap does not appear to act as a fully independent variable like it does for the Lo-Z MITL shots.

**VII. Summary and conclusions.** SMP diode experiments on RITS-6 were conducted under two operational conditions: a) the SMP diode load was driven by an IVA-MITL, resulting in flow current that is added to the diode current; and b) a relatively large range of output voltages was investigated, from a low of 3.5 MV to a high exceeding 11 MV in magnitude. In order to span this large range of output voltage, two separate inner MITL conductors were fielded: a larger-diameter MITL, known as the Lo-Z MITL, and a smaller-diameter MITL, known as the Hi-Z MITL. The Hi-Z MITL resulted in shots with higher output voltage and lower output current, and was fielded to investigate the voltage range between  $\sim 8.5$  and  $\sim 12$  MV. SMP experiments undertaken using the Lo-Z MITL have already been extensively discussed in previous publications. In general, the addition of the flow impedance resulted in relatively small changes to diode behavior compared to what may be termed “baseline operation” using a high-voltage interface as the source of forward-going power, i.e. where flow current does not occur. This appears so despite the fact that the flow current, intended to be diverted from the diode region by the use

of the knob, instead returns in proximity to the diode load after a short delay ( $\sim 20$  ns out of 70 ns). One set of experiments that suggested a different kind of diode operation was when the diode region was subjected to DC heating and RF discharge cleaning [9,10] in order to lower the contaminant population and extend the radiation pulse, particularly for smaller-diameter cathodes. While activation measurements validated the removal of the proton portion (the biggest ion fraction) from the counterstreaming ion population [28], the diode impedance did not increase, as might be expected. In the case of the larger heated/cleaned 12.5-12 configuration tested, the diode impedance actually *decreased*. When the smaller 8.5 – 8.3 configuration was heated, the diode impedance remained the *same*, despite the fact that the radiation pulsewidth was observed to increase. This unexpected behavior hinted at something unusual about the IVA-MITL-SMP combination with the Lo-Z MITL in place. With the Hi-Z MITL in place, the set of unusual behaviors increased, and is of course the subject of this paper.

Experiments conducted with the HI-Z MITL in place were characterized by behaviors that proved more problematic to understand, compared to the Lo-Z MITL experiments. These can be summarized as follows:

- 1) Large retrapping wave on the MITL bound current, indicating at least initial coupling to a load impedance significantly undermatched to the MITL impedance.
- 2) A decreasing level of diode current with time on many shots. This had not been observed on Lo-Z MITL shots. This occurred even as the overall level of current was steady or rising with time.
- 3) For the 12.5 – 12 diode configuration, the design carried over from the Lo-Z MITL experiments, every shot resulted in sudden increases in diode current later in the power pulse indicative of a premature impedance collapse. While such collapses were seen with the Lo-Z MITL, the behavior largely ceased when cathode dimensions larger than 8.5 mm were fielded. Since at the time of these experiments, such collapse was ascribed primarily to advancing electrode plasmas leading to the shorting of the diode electric field, the choice was made to increase the diode diameter and A-K gap, holding to a 1:1 aspect ratio, in order to address the indicated impedance collapse. Configurations with cathode diameters and respective A-K gaps of 14 mm (“14-14”), 17 mm (“17-17”), and 20 mm (“20-20”) were fielded. The 14-14 shots were observed to undergo similar current inflections as the 12.5-12 shots. The 17-17 shots, and lone 20-20 shot fielded, all showed a lack of current inflections, and their radiation pulses lasted through the entire power pulse.
- 4) It was observed anecdotally that signs of voltage stress were evident throughout the region illustrated schematically in Fig. 3. These include arc spots and discoloration of metal in any number of locations. As a result, the decision was made to reduce the RITS-6 Marx charge from 80 kV, the

standard for the Lo-Z MITL experiments, to 73 kV. This limited the ultimate dose and dose-rate of the Hi-Z MITL shots as compared with the Lo-Z MITL shots.

With the increase in the cathode diameter to 17 mm and then 20 mm, the resulting radiation pulse FWHM increased from  $\sim 30$  ns in the case of both the 12.5-12 and 14-14 shots, to the mid-40 ns range for the 17-17 shots taken, and to 51 ns for the lone 20-20 shot. The resulting doses @ 1 meter increased as well. However, because of the reduced Marx charge (see above), the maximum dose seen using the Hi-Z MITL (516 Rads @ 1 meter with Shot 1895 (17-17)) did not reach the highest dose level seen with the Lo-Z MITL (535 Rads @ 1 meter, 12.5-12 configuration). Thus the promise of higher radiation output with the Hi-Z MITL was not realized. Furthermore, the observed radiographic spot size also increased compared to the Lo-Z MITL shots. The single 20-20 shot was not repeated, largely because the resulting spot size was too large to measure with any accuracy.

The presence of the sizable retrapping wave on all the Hi-Z MITL shots renders the normal method of calculating corrected diode voltage (Eqs. 2 and 3) invalid, as discussed in Section III. An alternate method of estimating diode voltage is presented in Section III, which relies on the fundamental accuracy of the various PIN dose-rates plus the  $IV^x$  scaling of the dose-rate as previously derived [13], with empirical adjustments to the  $45^\circ$  and  $95^\circ$  directions ascribable to the influence of scattered photons in those observation directions. The resultant two-piece voltage estimate is shown to be consistent with the  $IV^{1.8}$  scaling for PIN\_45, and yield estimates (through cubic scaling as described in Section II) for the electron angle on the converter ( $\sim 20 - 40^\circ$ ) that are consistent with those observed in the Lo-Z MITL experiments. The derived voltage estimates are shown to be reasonably consistent with load voltage estimates calculated using Eq. 6 [27]. It is thus concluded that the derived estimate for the diode voltage is both qualitatively as well as quantitatively accurate.

The derived voltage estimate is then used to address the phenomenon of an indicated decrease in diode current with time. One mechanism put forth, that of knob emission (launched current from the knob due to the higher voltage stress in Hi-Z MITL shots) could prove to be problematic in any experiment where space in the diode region is limited, and/or where high voltage stress is encountered. Both the  $IV^x$  scaling of the PIN dose-rates, plus an analysis of the lower-voltage shot series in which the estimated stress is lower than that encountered on the Lo-Z MITL shots, tend to indicate that while knob emission may well have occurred, the current so produced did not affect the radiation output, as the current flowing through the diode (IBEAM) is concluded to be the source of the radiation dose.

Another explanation for the diode current decrease is explored with the calculation of the three system impedances:  $Z_{\text{IBEAM}}$ ,  $Z_{\text{TOTAL}}$ , and  $Z_{\text{PARALLEL}}$ . The collection of  $Z_{\text{TOTAL}}$  waveforms (Fig. 2) is used to infer an operational rule of the IVA-MITL architecture: that the generator produces a current consistent with the flow impedance of the MITL used. The data in Fig. 2 are derived from Lo-Z MITL shots. If the rule is correct, then one would expect to see  $Z_{\text{TOTAL}}$ s from Hi-Z MITL shots that track at approximately 80 ohms, the flow impedance of the Hi-Z MITL. With the calculation of  $Z_{\text{TOTAL}}$  using the derived voltage estimate, this is indeed what happens (Figs. 18a-b and 25a-b). Then if one assumes that the derived diode voltage estimate is correct, and  $Z_{\text{TOTAL}}$  is fixed at a level consistent with the 80-ohm flow impedance, then  $Z_{\text{LOAD}}$  must rise and diode current must fall with time. Note that this statement is a mathematical one, and contains no causality. In fact, one interpretation is that knob emission *does* in fact occur, but as an organized rather than a chaotic process. That is, a hypothetical knob emission could generate enough flow impedance to restore a predetermined ratio between the flow and the diode current. Indeed, a similar “MITL” emission occurs in which enough flow impedance is generated (once the MITL voltage stress exceeds the emission threshold) to be consistent with the MITL flow impedance. What complicates the situation here is that the diode generates its own level of current through its own adjustable parameters (A-K gap, for instance). If this level of current is inconsistent with the overall level of total current (flow plus diode), then the diode current must change. Note that this could occur for any diode load that operates with its own physics rules. On a typical Hi-Z MITL shot (see Fig. 21a), the SMP diode region operates such that at the beginning of the power pulse, there is almost no sheath current. During the power pulse, diode current is then converted to flow current. This is the opposite of that predicted in References 27 and 28, and the opposite of that observed with Lo-Z MITL shots, In the latter,  $Z_{\text{PARALLEL}}$  rises as flow current is converted to diode current (see Fig. 19).

The implications of these statements for determining (and setting) such experimental factors such as diode impedance are significant. The indicated diode impedance, for the 12.5 – 12 diode, appears to be higher with the use of the Hi-Z MITL (80 ohms compared to ~ 65 ohms (initial) at Lo-Z [9-11]). Thus, it appears that diode impedance depends upon the level of flow impedance of the IVA. The diode impedance is also seen to rise during the pulse, as well as stay constant. Neither behavior is observed at Lo-Z, and implies that conventional explanations of electrode gap closure are not sufficient to explain the observed diode behavior. Another feature of dose-rate behavior is the presence of short time-scale “spikes” that have been noted on some shots. The suddenness of the spikes in time are not consistent with angle change, and instead may signal the presence of electron strikes to the anode that may have been observed by one of the PINs, but not the other(s). As we have seen in the analysis above, the presence of spikes has been discounted in constructing a voltage estimate.

These conclusions seem radical compared to operation of diodes attached to high-voltage interfaces. Further experiments by other researchers could be useful in validating the conclusions drawn here. Left unresolved in this picture is the cause of the premature impedance collapse seen with the 12.5 – 12 and 14 – 14 diodes. In the case of the Lo-Z MITL experiments [9,10], two mechanisms for this behavior are suggested: 1) gap closure due to electrode plasma motion, and 2) fast-developing oscillations in the electron angle to the converter that are inferred to lead to impedance collapse. The Hi-Z data do not clearly point to the oscillation mechanism. The question of electrode plasma behavior was not systematically investigated with the Hi-Z MITL shots, but if electrode gap closure were to be found as the causal mechanism for the 12-5-12 and 14-14 SMP shots, the implication would be that the cathode/anode plasma convergence velocities must be significantly higher than those inferred for the Lo-Z MITL shots. As was already pointed out in connection with Fig. 25b, if any electrode gap closure occurs in the Hi-Z MITL shots, it is not immediately evident. Also, it is observed anecdotally that in many of the 12.5–12 and 14-14 shots taken with the Hi-Z MITL in place, and which exhibited premature impedance collapse, the inferred electron angle [13] is indicated to steepen considerably later in the power pulse, and therefore it is suggested that this steepening could in fact contribute to the premature impedance collapse observed on these shots. Such angle behavior was also inferred for Shot 1884 (not shown), increasing to 80° and beyond later in the pulse. This shot, like all 12.5 – 12 shots taken with the Hi-Z MITL, also exhibited premature impedance collapse. At this point, however, pending further investigation, the angle steepening can at most be regarded as an anecdotal observation and not as a confirmed cause of the impedance collapse.

Another implication of this systems-oriented approach is that simulations of IVA-diode behavior (the diode can be generalized beyond just an SMP) that only include a posited forward-going voltage without inclusion of the IVA electron flow will likely not yield correct results.

As mentioned already [27,28], it has been argued the operating a Hi-Z MITL load into an undermatched load is a viable way of conducting SMP experiments. Our experience with such a configuration as operated on RITS-6 does not validate this assumption. One might argue that increasing the knob-dustbin distance could mitigate the voltage stresses that could cause the knob emission, if such emission is in fact occurring. Another option is to increase the size of the dustbin. Given that the present dustbin used is quite large, the result would be considerably increased facility size, as well as increased lumped inductance that accompanies the bigger size. Another option is to decrease the knob size, since it has been demonstrated by comparing total G current with  $I_A$  that the knob diverts little or no current in the Hi-Z

configuration. Data from the Lo-Z MITL experiments clearly suggest that the same level of undermatching produces more benign results in the case of the Lo-Z MITL. This leads to the hypothesis, not validated at this time, that not only is the ratio of load-to-flow impedance important, but the *absolute level* of flow impedance may matter. That is, better performance may be expected in general if the MITL flow impedance of the IVA is kept below say 60 ohms. This hypothesis might be a very interesting topic for future IVA-diode work.

There does appear to be one design path that would probably lead to a successful SMP operation at high voltage. That would be an IVA with a Lo-Z MITL, but designed for say  $> 15$  MV operation. Such a machine exists today in the HERMES-III facility at Sandia National Laboratories (18 MV, 650 kA, 34 ohms vacuum impedance, 40 ns). Its size is considerably larger than the already-large RITS-6 facility.

## **ACKNOWLEDGEMENTS**

The authors acknowledge the technical support of the RITS-6 facility staff – Dan Nielsen, Derek Ziska, Bill Bui, Steve Cordova, Robert Obregon, Frank Wilkins, and Ray Gignac. Darryl Droemer provided key diagnostic support. The authors also gratefully acknowledge the role of Dr. Bruce Weber of the Naval Research Laboratory in the execution of the ITS-CYLTRAN simulations required to create the cubic scaling modification to radiation scaling, as well as construction of the plots seen in Figs. 6, 7, 8, 16, and 20. Sandia National Laboratories is a multimission laboratory managed and operated by National Technology and Engineering Solutions of Sandia, LLC, a wholly owned subsidiary of Honeywell International, Inc., for the U.S. Department of Energy’s National Nuclear Security Administration under contract DE-NA0003525. The views in this paper are not necessarily the views of Sandia National Laboratories or DOE/NNSA. Data from which conclusions were reached in this paper is available upon request.

### **Data Availability Statement**

The data that support the findings of this study are available from the corresponding author upon reasonable request.

## REFERENCES

1. G. S. Cunningham and C. Morris, *The Development of Flash Radiography*, Los Alamos Science, Number 28 (2003).
2. Consult the excellent review article: J. Maenchen, G. Cooperstein, J. O'Malley, and I. Smith, *Advances in Pulsed Power-Driven Radiography*, Proc. IEEE 92, 1021 (2004): and references listed therein.
3. M. S. Di Capua and D. G. Pellinen, *Propagation of power pulses in magnetically insulated vacuum transmission lines*, J. Appl. Phys **50** (1979) 3713 – 3720.
4. See, for example,  
<http://www.pulsedpower.net/Applets/Electromagnetics/CoaxialSection/CoaxialSection.html>
5. P. A. Miller and C. W. Mendel, *Analytic model of applied-B ion diode impedance behavior*, J. Appl. Phys. **61** (1987) 529-539.
6. P. F. Ottinger and J. W. Schumer, *Rescaling of equilibrium magnetically insulated flow theory based upon results from particle-in-cell simulations*, Phys. Plasmas **13** (2006) 063109-1 – 17.
7. P. F. Ottinger, T. J. Renk, and J. W. Schumer, *Method for improved voltage determination for pulsed power systems utilizing a magnetically insulated transmission line*, Phys. Plasmas **26**, 023105 (2019).
8. R. J. Allen, R. J. Commisso, G. Cooperstein, P. F. Ottinger and J. W. Schumer, *Extension of the operating point of the Mercury IVA from 6 to 8 MV*, 2011 IEEE Pulsed Power Conference, Chicago, IL, 2011, pp. 1036-1041, doi: **10.1109/PPC.2011.6191638**.
9. T. J. Renk, M. L. Kiefer, B. V. Oliver, T. J. Webb, J. J. Leckbee, M. D. Johnston, S. Simpson, and M. G. Mazarakis, *Characterization of Self-Magnetic Pinch (SMP) radiographic diode performance on RITS-6 at Sandia National Laboratories: 1) Diode Dynamics, DC Heating to extend Radiation Pulse*, Phys. Plasmas xxx, and references therein.
10. Timothy J. Renk, Bryan V. Oliver, Mark L. Kiefer, Timothy J. Webb, Joshua J. Leckbee, Mark D. Johnston, Sean Simpson, and Michael G. Mazarakis, *Characterization of Self-Magnetic Pinch (SMP) radiographic diode performance on RITS-6 at Sandia National Laboratories: 1) Diode Dynamics, DC Heating to extend Radiation Pulse*, Sandia Report SAND-2021-13998, October 2021.
11. K.D. Hahn, N. Bruner, M.D. Johnston, B.V. Oliver, T. J. Webb, D.R. Welch, S.R. Cordova, I. Crotch, R.E. Gignac, J.J. Leckbee, I. Molina, S. Portillo, J.R. Threadgold, D. Ziska, *Overview of Self-Magnetically Pinched-Diode Investigations on RITS-6*, IEEE Trans. Plasma Sci. **38**, 2652 (2010).
12. N. Bruner, D. R. Welch, T. J. Webb, M. G. Mazarakis, M. L. Kiefer, M. D. Crain, D. W. Droemer, R. E. Gignac, M. D. Johnston, J. J. Leckbee, I. Molina, D. Nielsen, R. Obregon, T. Romero, S. Simpson, C. C. Smith, F. L. Wilkins, D. Ziska, *The impact of plasma dynamics on the self-magnetic-pinch diode impedance*, Phys. Plasmas **22** (2015) 033113-1 – 10.

13. T. J. Renk, B. V. Weber, I. M. Rittersdorf, and T. J. Webb, *Technique for inferring angle change as a function of time for high-current electron beams using a dose-rate monitor array*, Rev. Sci. Instrum. **90**, 114709 (2019).
14. T. J. Renk, P. F. Ottinger, and R. E. Durrer, *Production of pulsed high-energy neutron bursts from beam-target interaction using a 15 MeV HERMES III ion beam*, AIP Advances **10**, 125106 (2020).
15. ).
16. T. J. Renk, P. F. Ottinger, and R. E. Durrer, *Development of Fast-Pulse Neutron Generation Capability by Beam-Target Interaction on HERMES-III for Radiation Effects Testing: Final Report*, Sandia Report SAND2019-14443, Sandia National Laboratories, December 2019.
17. N. Bruner, D. R. Welch, T. J. Webb, M. G. Mazarakis, M. L. Kiefer, M. D. Crain, D. W. Droemer, R. E. Gignac, M. D. Johnston, J. J. Leckbee, I. Molina, D. Nielsen, R. Obregon, T. Romero, S. Simpson, C. C. Smith, F. L. Wilkins, D. Ziska, *The impact of plasma dynamics on the self-magnetic-pinch diode impedance*, Phys. Plasmas **22** (2015) 033113-1 – 10.
18. V. L. Bailey, P. A. Corcoran, D. L. Johnson, I. D. Smith, J. E. Maenchen, K. D. Hahn, I. Molina, D. C. Rovang, S. Portillo, E. A. Puetz, B. V. Oliver, D. V. Rose, D. R. Welch, D. W. Droemer, and T. L. Guy, in *Proceedings of the 15th International Conference on High-Power Particle Beams, St. Petersburg, Russia, July 2004*, edited by V. Engelko, G. Mesyats, and V. Smirnov (ISBN 5-87911-088-5, D. V. Efremov Scientific Research Institute of Electrophysical Apparatus, St. Petersburg, Russia, 2004), p. 247.
19. I. Crotch, *Radiographer's equations for megavolt electron beams*, IEEE Conference on Plasma Science (ICOPS 2004), p. 183.
20. P. N. Martin, J. R. Threadgold, A. Jones, J. McLean, G. M. Cooper, K. Webb, G. Jeffries, P. Juniper, *Investigations into the Role of the Bremsstrahlung Conversion Target in the Self-Magnetic Pinch Radiographic Diode*, IEEE Trans. Plasma Sci **39** (2011) 1943 – 48.
21. T.W.L. Sanford, J. A. Halbleib, J. W. Poukey, A. L. Pregonzer, R. C. Pate, C. E. Heath, R. Mock, G. A. Mastin, D. C. Ghiglia, T. J. Roemer, P. W. Spence, G. A. Proulx, *Measurement of electron-energy deposition necessary to form an anode plasma in Ta, Ti, and C for coaxial bremsstrahlung diodes*, J. Appl. Phys. **66**(1) (1989), pp. 10-22.
22. A. E. Blaugrund, G. Cooperstein, S. A. Goldstein, *Relativistic electron beam pinch formation processes in low impedance diodes*, Phys. Fluids **20** (1977) 1185–1194.
23. LSP is a software product of ATK Mission Research, Albuquerque, NM.
24. Dale R. Welch, David V. Rose, Nichelle Bruner, Robert E. Clark, Bryan V. Oliver, Kelly D. Hahn, and Mark D. Johnston, *Hybrid simulation of electrode plasmas in high-power diodes*, Phys. Plasmas **16** (2009), 123102-1 - 9.
25. J. A. Halbleib and T. A. Mehlhorn, ITS: The integrated TIGER series of coupled electron/photon Monte Carlo transport codes, Nucl. Sci Eng. **92** (2) (1986), 338.

26. D. Hinshelwood, R. Allen, R. Comisso, G. Cooperstein, B. Huhman, D. Mosher, D. Murphy, P. F. Ottinger, J. Schumer, S. Swanekamp, S. Stephanakis, B. Weber, F. Young, I. Crotch, J. O'Malley, and J. Threadgold, *IEEE Trans. Plasma Sci.* **35** (2007) 565.
27. D. Hinshelwood, G. Cooperstein, D. Mosher, D. Ponce, S. Strasburg, S. Swanekamp, B. Weber, F. Young, A. Critchley, I. Crotch, and J. Threadgold, *IEEE Trans. Plasma Sci.* **33** (2005) 696.
28. V. L. Bailey, D. L. Johnson, P. Corcoran, I. Smith, J. E. Maenchen, I. Molina, K. Hahn, D. Rovang, S. Portillo, B. V. Oliver, D. Rose, D. Welsh, D. Droemer, and T. Guy, in 14<sup>th</sup> International Pulsed Power Conference (**PPC-2003**), Dallas, TX, 2003, M. Giesselman and A. Neuber, Eds., ISBN 0-7803-7915-2, 399-402.
29. V. Bailey et al, in 15<sup>th</sup> International Conference on High-Power Particle Beams (Beams 2004), St. Petersburg, Russia, 2004, Gennady Mesyats, Valentin Smirnov, Vladimir Engelko, Eds, ISBN 5-87911-088-5, 247-250.
30. M. G. Mazarakis, N. Bennett, M. E. Cuneo, S. D. Fournier, M. D. Johnston, M. L. Kiefer, J. J. Leckbee, D. S. Nielsen, B. V. Oliver, M. E. Sceiford, S. C. Simpson, T. J. Renk, C. L. Ruiz, T. J. Webb, D. Ziska, D. W. Droemer, R. E. Gignac, R.J. Obregon, F. L. Wilkins, D. R. Welch, *Contribution of the backstreaming ions to the self-magnetic pinch (SMP) diode current*, *Phys. Plasmas* **25** (2018), 043508 -1 to 9.

## FIGURE CAPTIONS

- Fig. 1. a. SMP MITL flow, Stage 1. b. Stage-2. c. Stage 3.
- Fig. 2.  $Z_{TOTAL}$  for various shots taken with the Lo-Z MITL.
- Fig. 3. Schematic diagram of the RITS-6 downstream MITL and SMP load region.
- Fig. 4. Closeup schematic view of the SMP diode and A-K gap.
- Fig. 5. Schematic top view of the RITS cell: includes converter package, PIN detector locations, and materials between the photon source and the PIN locations attenuating the photon flux. (Drawing not to scale.) Reproduced from [T. J. Renk, B. V. Weber, I. M. Rittersdorf, T. J. Webb, Rev. Sci Instrum. **90** (2019) 114709], with the permission of AIP Publishing.
- Fig. 6. Fit of ITS output to dose and electron energy using a) power-law scaling  $cIV^x$  and b) cubic scaling.
- Fig. 7. Inferred electron angle for Shot 1861 using axial dose-rate overlaid on angle contours using a) power-law scaling and b) cubic scaling.
- Fig. 8. Inferred electron angle vs. time for Lo-Z Shot 1908 using power-law scaling ( $\text{angle}(t)$ ) as compared to cubic scaling ( $\text{angle}IV^x$ ).
- Fig. 9. Schematic drawing of the comparison of the Lo-Z and Hi-Z MITL (center conductor) as installed on RITS. The field-shaper knob and SMP diode configuration are the same for both MITLs.
- Fig. 10. Total and bound current at position E, Shots 1977 (Lo-Z) and 1884 (Hi-Z).
- Fig. 11a. Total (BLACK) and bound (RED) currents, LSP prediction, 2 meters upstream from HERMES ion diode load. Reproduced from [T. J. Renk, P. F. Ottinger, and R. E. Durrer, AIP Advances 10, 125106 (2020)], with the permission of AIP Publishing.
- Fig. 11b. BLACK curve: predicted MITL voltage 2 meters upstream from load. GREEN curve: predicted voltage across A-K gap. Reproduced from [T. J. Renk, P. F. Ottinger, and R. E. Durrer, AIP Advances 10, 125106 (2020)], with the permission of AIP Publishing.
- Fig. 12. a. Time-shifted total G current,  $I_A$ , and  $(G \text{ shifted} - I_A)$ , Shot 1908. b. Same waveforms, Shot 1889.
- Fig. 13. Shot 1861: PIN 95 (scaled), plotted with time-shifted currents at both positions E and F.

Fig. 14.a. Scaled PIN\_0, PIN\_45, and PIN\_95 waveforms, Shot 1861. b). Truncated time-shifted corrected Voltage at E scaled to power 1.1, and plotted with a (scaled) PIN\_95 waveform.

Fig. 15.a. Shot 1861: Two- piece composite voltage from E, compared to VCORR\_E without truncation. b). Two-piece composite voltage from E raised to 1.8 power, then scaled to PIN\_45.

Fig. 16.  $I_A$  and  $I_L$  currents, Shots 1977 and 1884.

Fig. 17.a. Diode region currents  $I_A$ ,  $I_L$ ,  $I_{UP}$ , net ( $I_A - I_L$ ), and (scaled) PIN\_0, Shot 1861. b. Four individual  $I_L$  monitor signals, Shot 1861.

Fig. 18.a.  $Z_{LOAD}$ ,  $Z_{TOTAL}$ , time-shifted Z at E, Shot 1861. b. Add (scaled) PIN\_0 and  $Z_{PARALLEL}$ .

Fig. 19.  $Z_{LOAD}$ ,  $Z_{TOTAL}$ ,  $Z_{PARALLEL}$ , timeshifted Z at E + Z at G, (scaled) PIN\_0, Shot 1977 (Lo-Z MITL).

Fig. 20.a. Bound current signals at E, F, G, IFEED, and IBEAM, Shot 1861. b. Same signals, Shot 1977 (Lo-Z MITL).

Fig. 21.a. Net sheath current at positions E, F, G, and  $I_L$ , Shot 1861 (Hi-Z MITL). b. Same currents, Shot 1908 (Lo-Z MITL).

Fig. 22. Sheath current at  $I_L$  position compared to ( $I_A - I_L$ ), Shot 1861.

Fig. 23.a.  $I_L$  and (scaled) PIN\_0 waveform, Shots 1908 and 1884. b. PIN\_0 dose rate in units of Krad/cm<sup>2</sup>/sec/Amp, Shots 1908 and 1884.

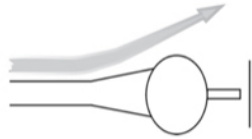
Fig. 24.a.  $V_{CORR}$ , Shots 1908 and 1884. b. Ratio of dose-rate/amp, Shots 1884 and 1908, plus  $V_{CORR}$  ratio, same shots raised to 2.34 power. Third curve is  $I_L$  for Shot 1884 (scaled).

Fig. 25.a.  $Z_{TOTAL}$ , Shots 1908 and 1884. Z at position G added for Shot 1908, Z at position E for Shot 1884, both time-shifted. b.  $Z_{LOAD}$ , Shot 1908 and 1884.

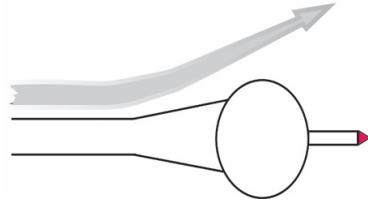
Fig. 26.a.  $I_L$  current and net ( $I_A - I_L$ ), Shots 1861, 1890, 1889. b.  $I_L$  currents, 4.5 MV series, various shots, (Lo-Z MITL).

Fig. 27.  $I_L$  and net ( $I_A - I_L$ ), Shots 1537, 1541, and 1549, 4.5 MV series, Lo-Z MITL.

Fig. 28.a. PIN\_0, Shots 1861, 1890, 1889. b.  $V_{CORR}$ , Shots 1861, 1890, 1889.



**Fig. 1a**



**Fig. 1b**

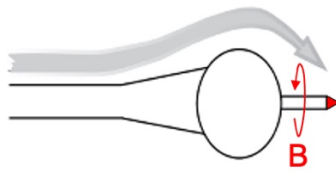


**Fig. 1c**

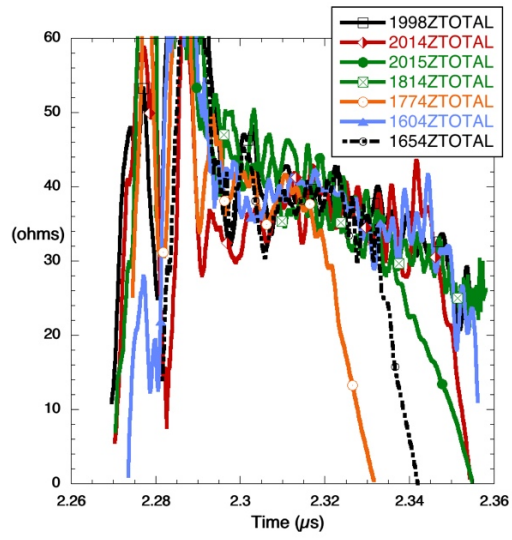


Fig. 2

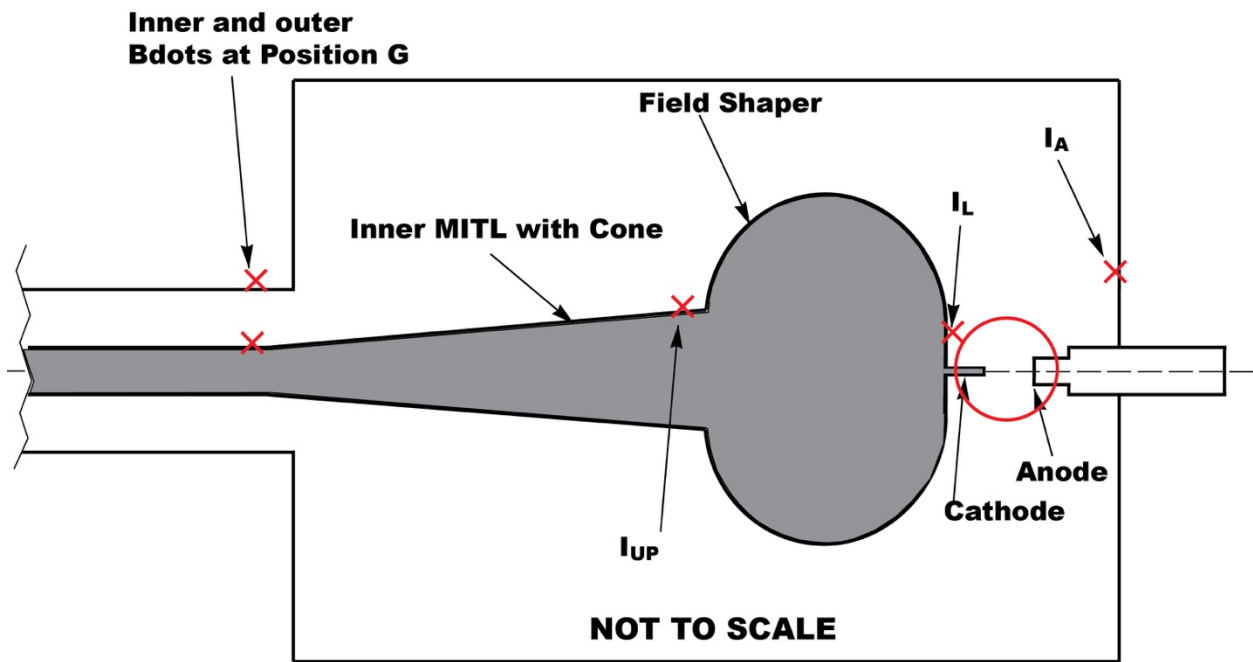


Fig. 3

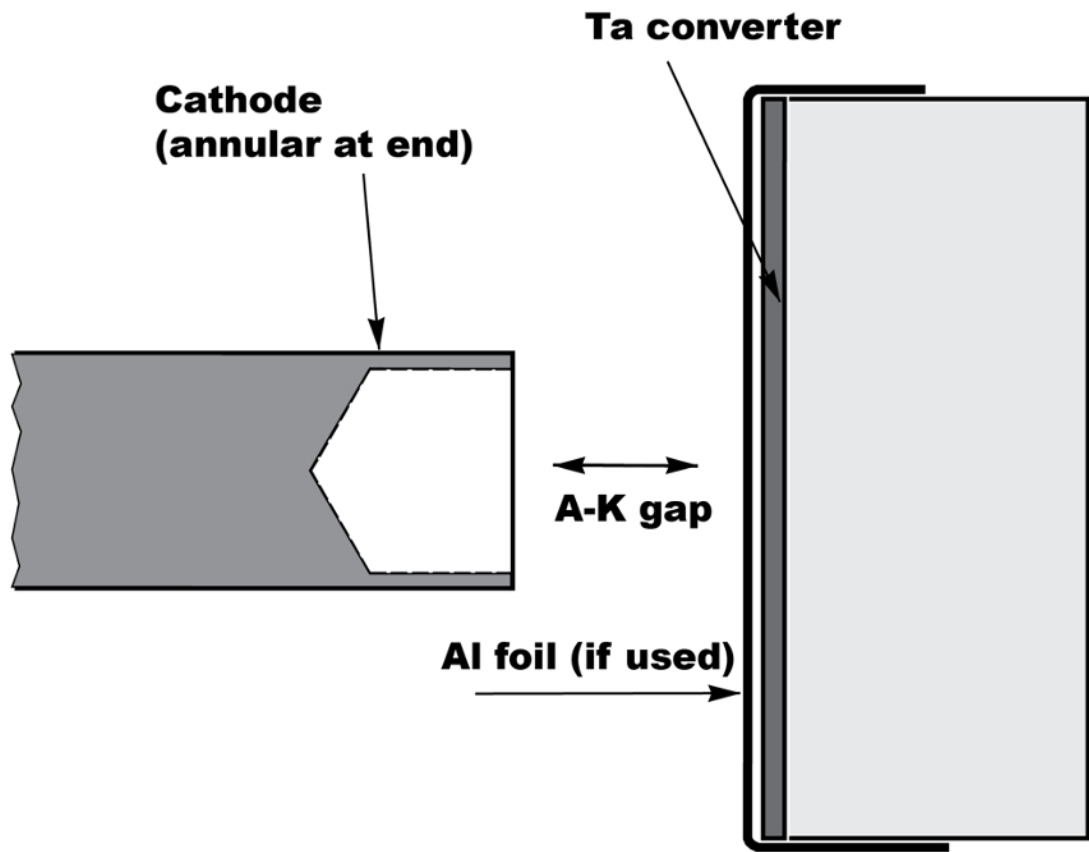


Fig. 4

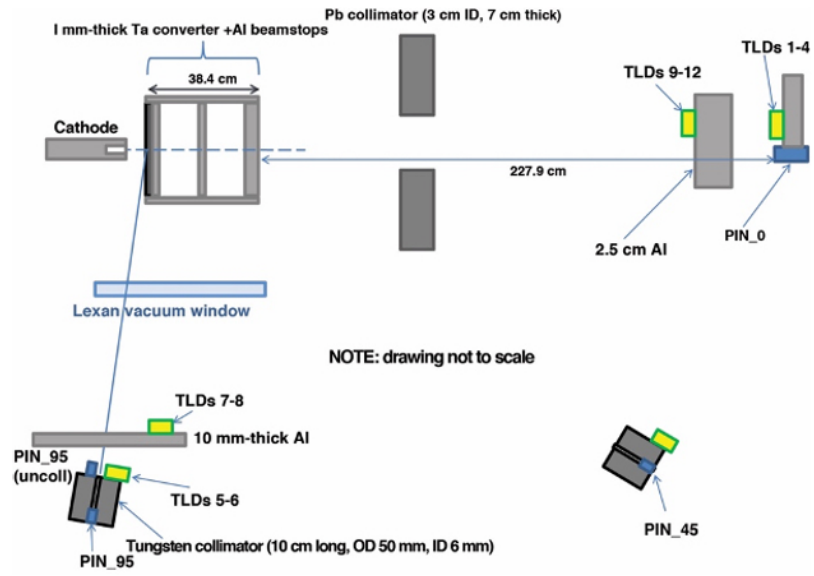


Fig. 5

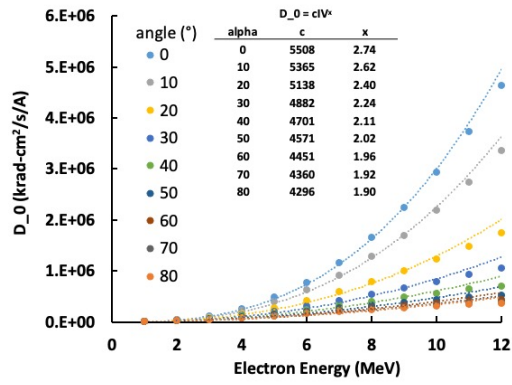


Fig. 6a

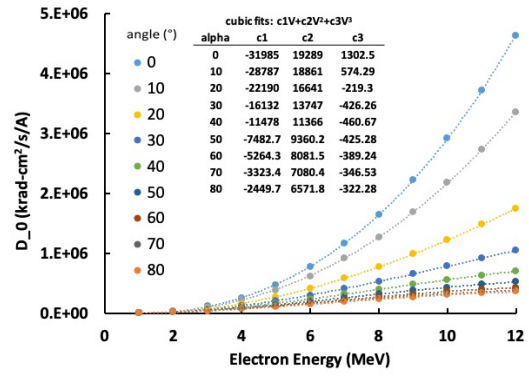
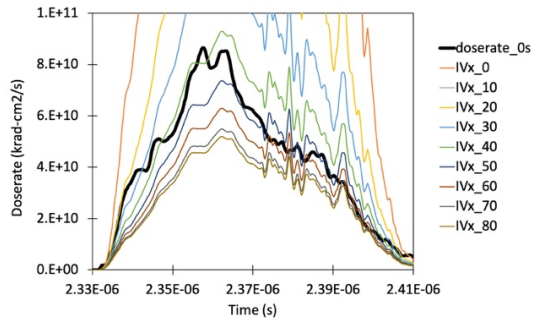
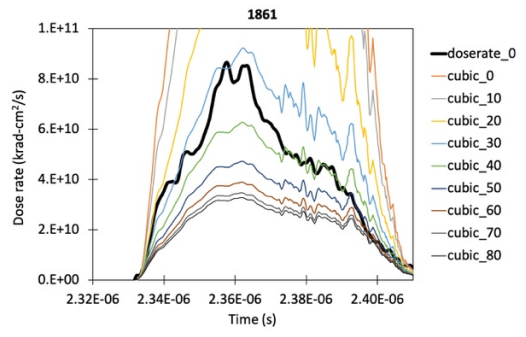


Fig. 6b



**Fig. 7a**



**Fig. 7b**

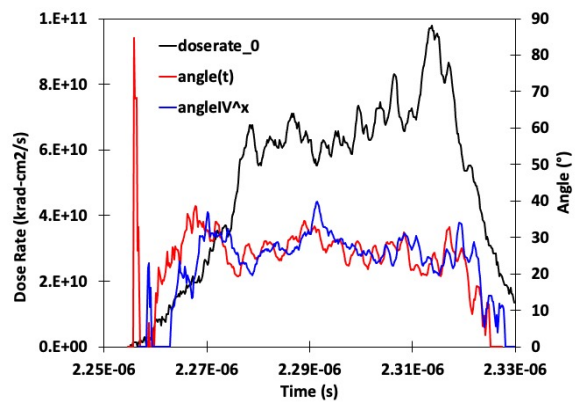


Fig. 8

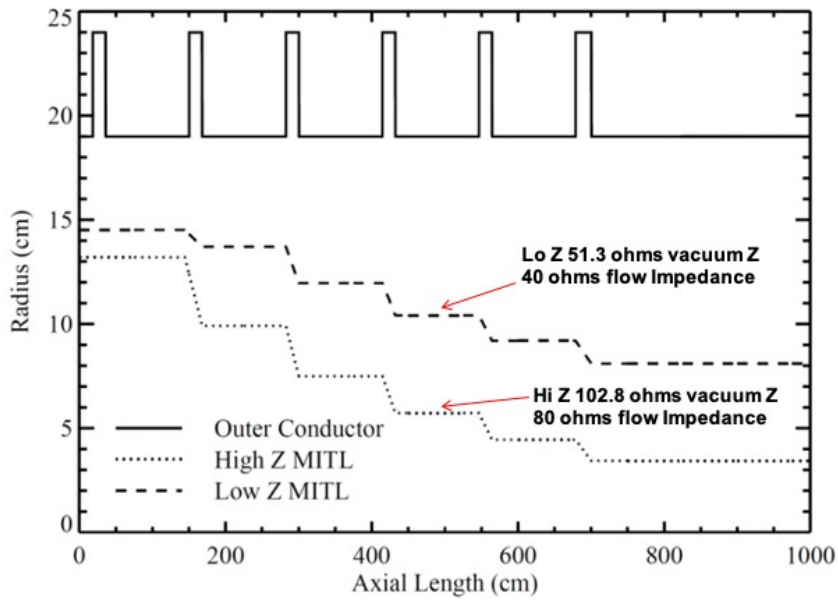


Fig. 9

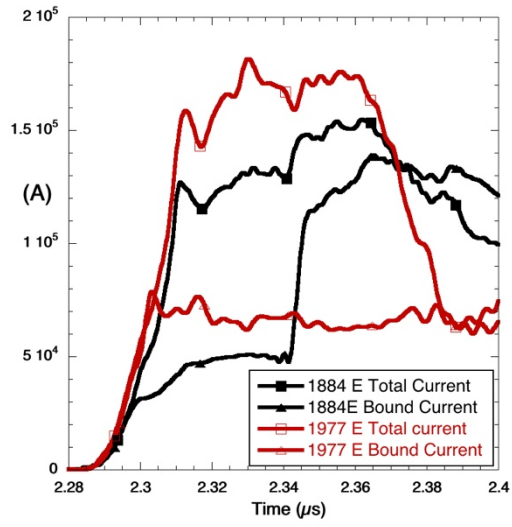
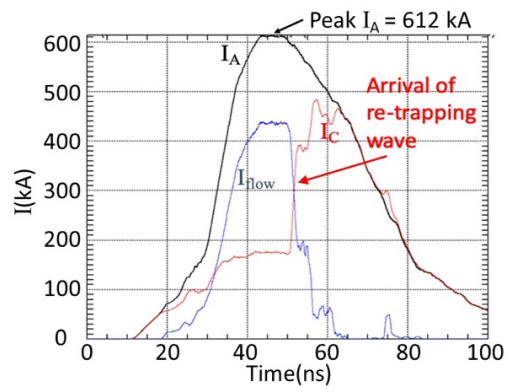
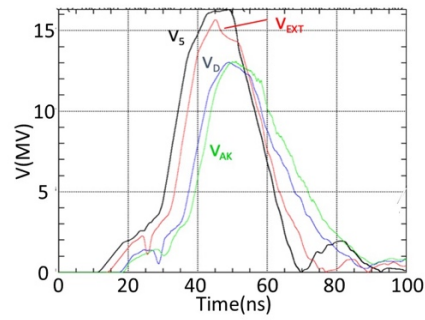


Fig. 10



**Fig. 11a**



**Fig. 11b**

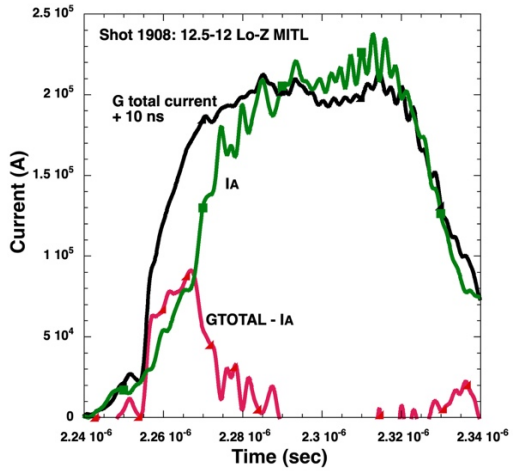


Fig. 12a

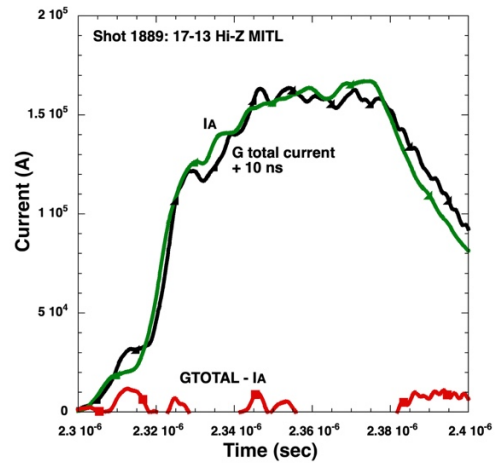


Fig. 12b

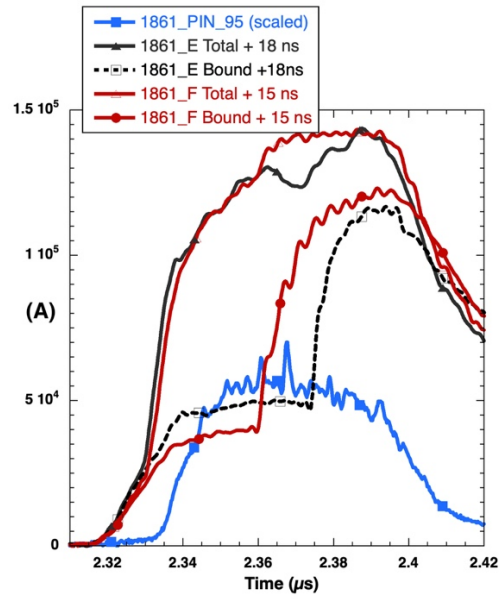


Fig. 13

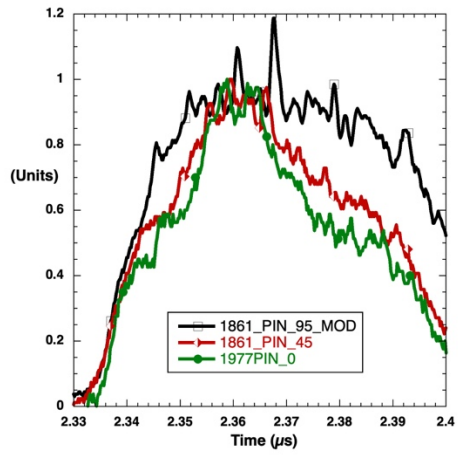


Fig. 14a

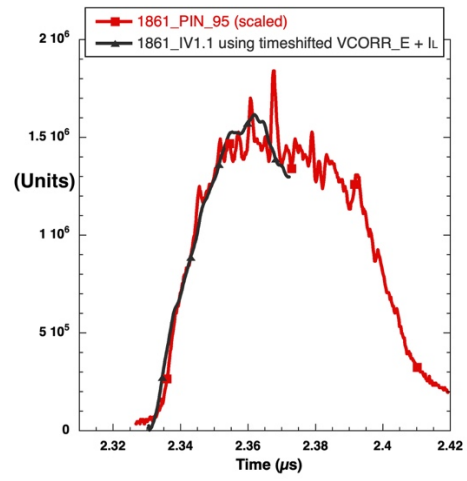


Fig. 14b

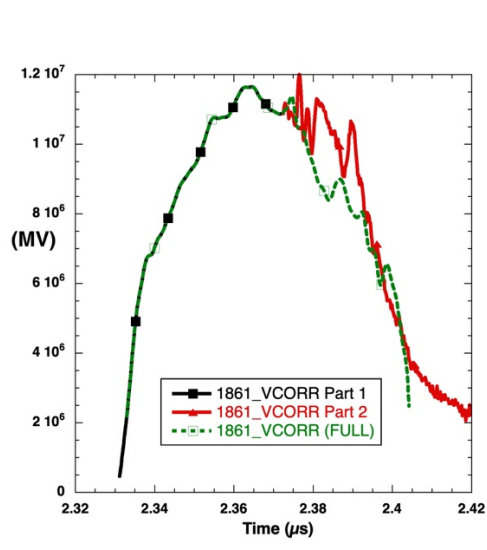


Fig. 15a

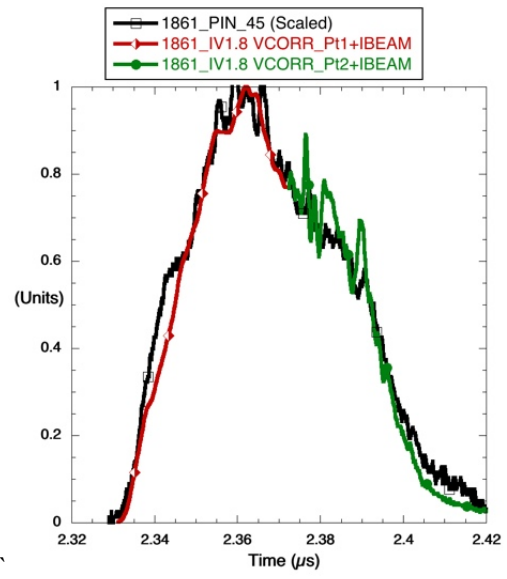


Fig. 15b

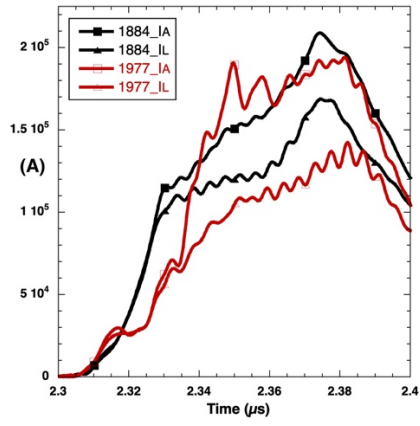


Fig. 16

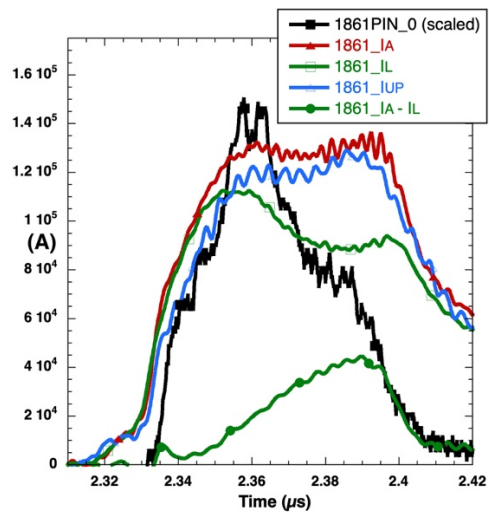


Fig. 17a

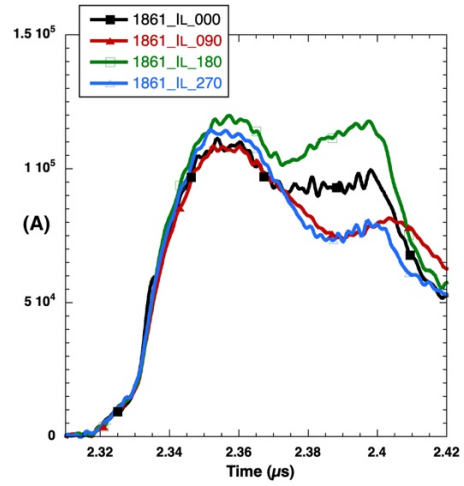


Fig. 17b

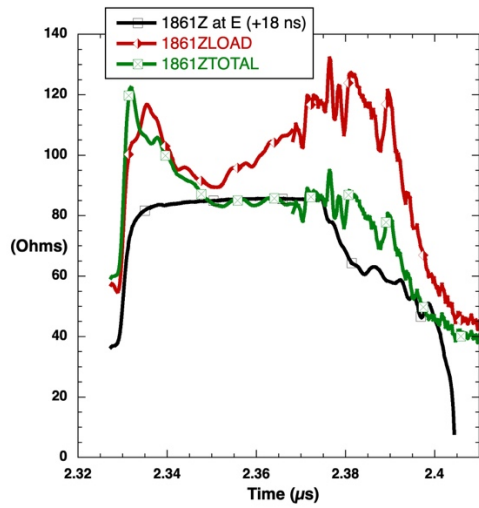


Fig. 18a

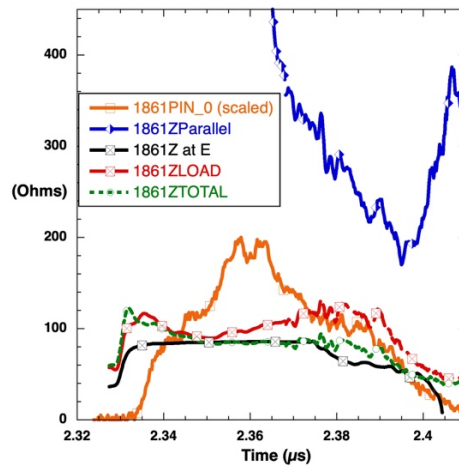


Fig. 18b

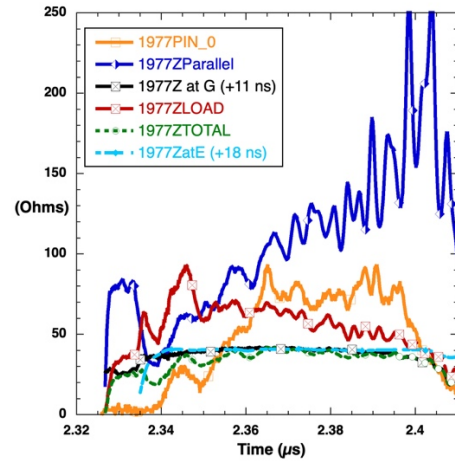


Fig. 19

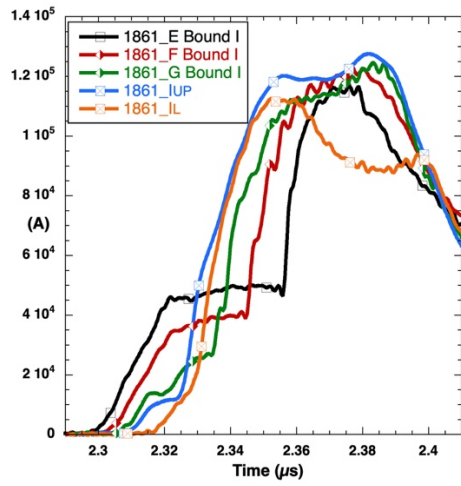


Fig. 20a

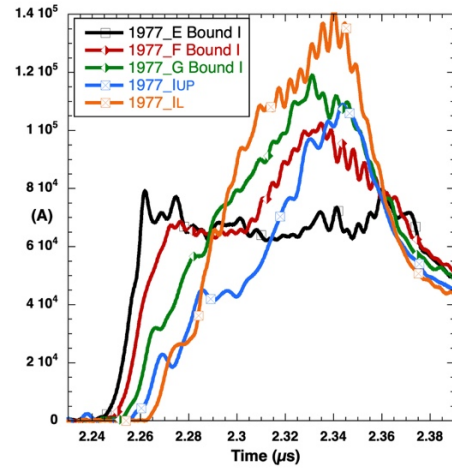


Fig. 20b

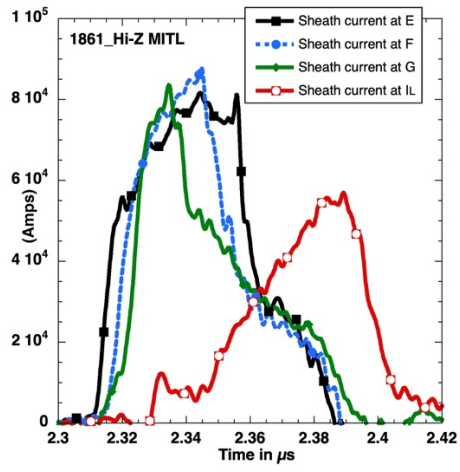


Fig. 21a

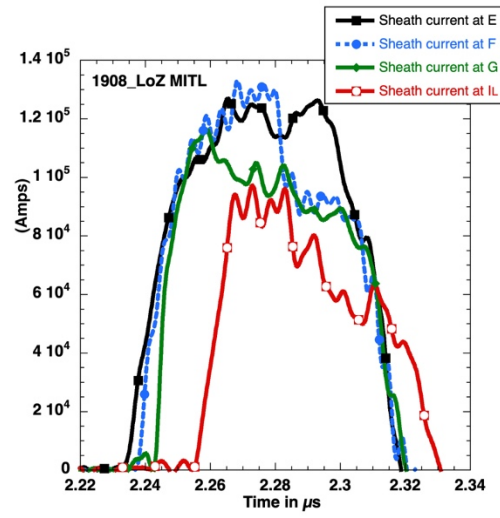


Fig. 21b

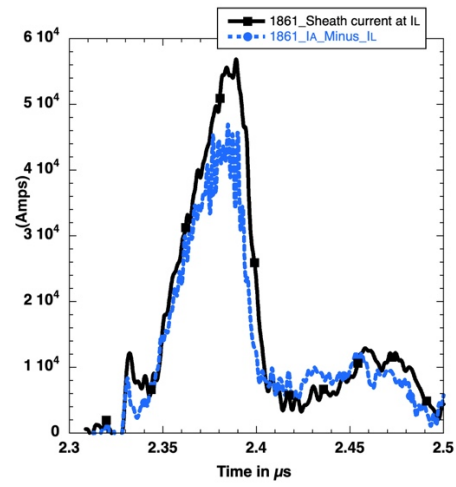


Fig. 22

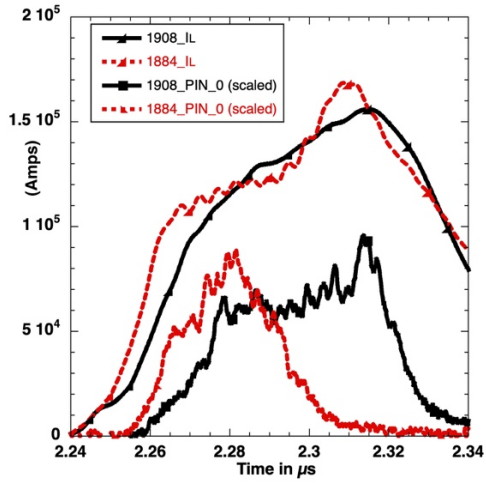


Fig. 23a

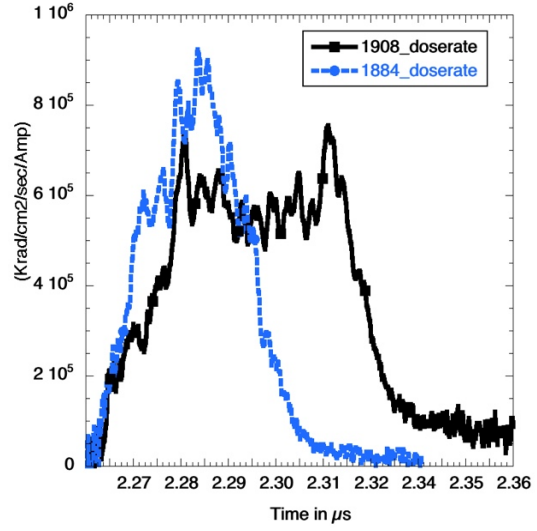


Fig. 23b

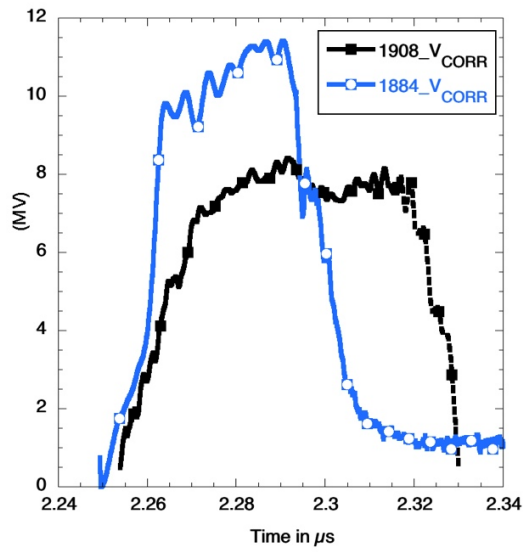


Fig. 24a

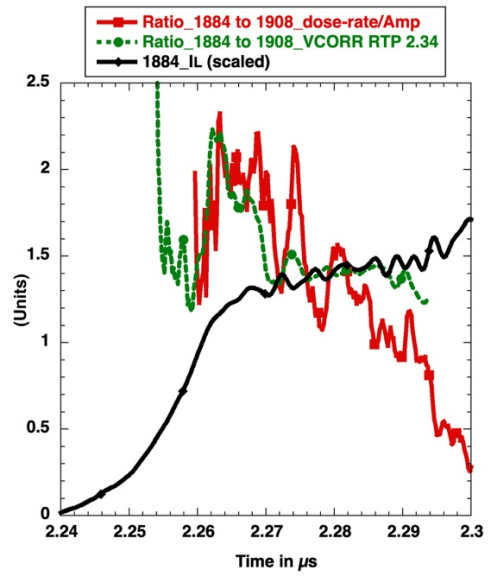


Fig. 24b

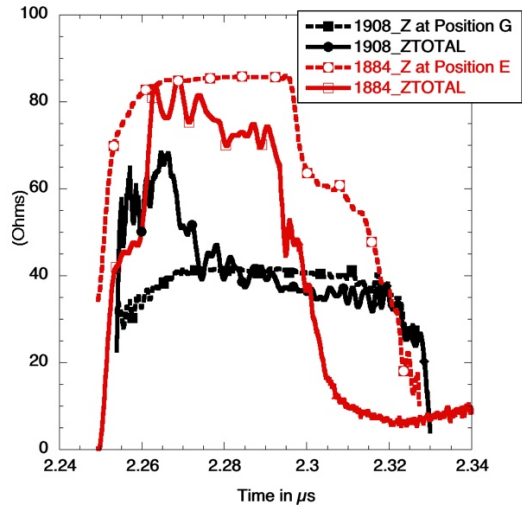


Fig. 25a

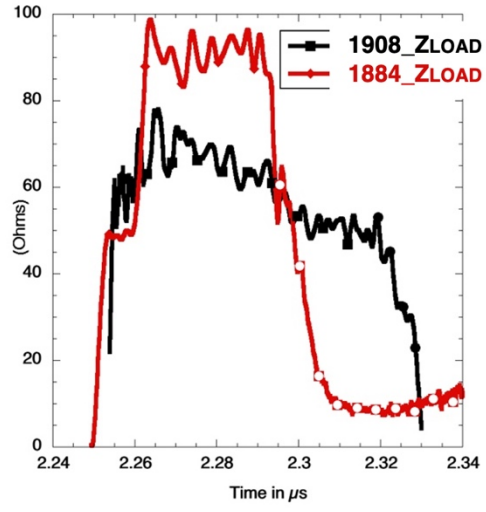


Fig. 25b

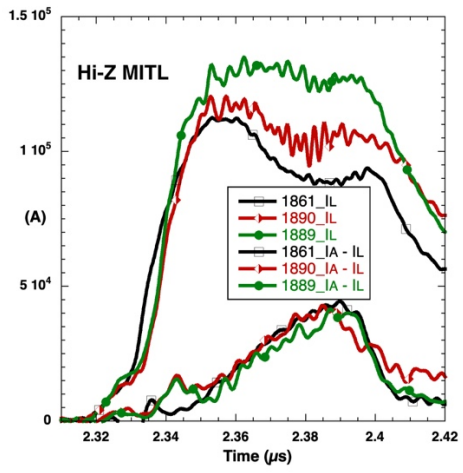


Fig. 26a

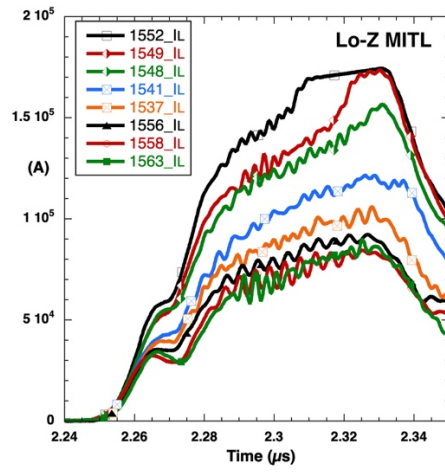


Fig. 26b

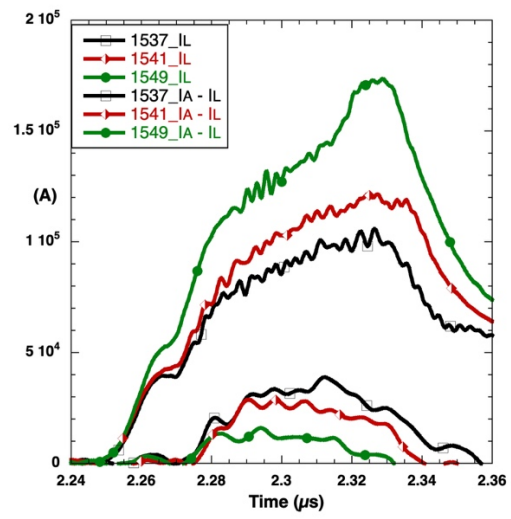


Fig. 27

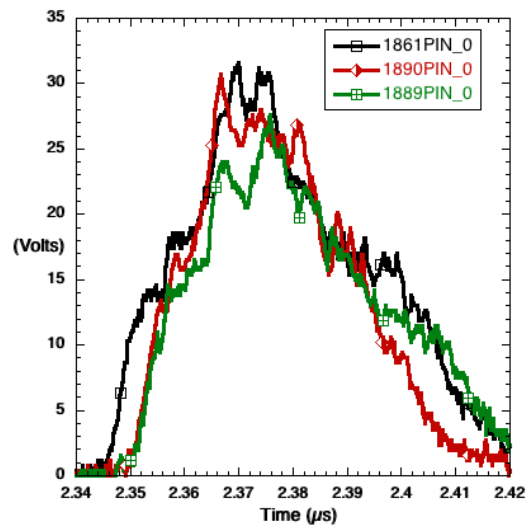


Fig. 28a

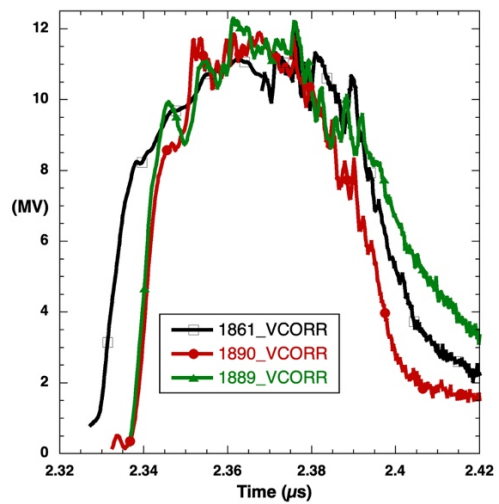


Fig. 28b